Microstructure observations of the summer-to-winter destratification at a coastal site in the Gulf of Naples.

Florian Kokoszka[1], Fabio Conversano[1], Daniele Iudicone[1], Bruno Ferron[2], Pascale Bouruet-Aubertot[3], Justine Mc Millan[4]

[1]Stazione Zoologica Anton Dohrn, Naples, Italy
[2]Univ. Brest, CNRS, IFREMER, IRD, Laboratoire d'Océanographie Physique et Spatiale (LOPS), IUEM, Plouzané, France
[3]Sorbonne Université (UPMC, Univ Paris 06)-CNRS-IRD-MNHN, LOCEAN, Paris, France
[4]Rockland Scientific International Inc., Victoria, Canada

Key Points:

- The seasonal cycle of the dissipation rates of turbulent kinetic energy ϵ at a mid-latitude coastal site is presented, covering the destratification period.
- A progressive deepening of the mixed layer depth was observed from September to December, finally extending to the whole water-column at the beginning of winter.
- The statistics of ϵ depend upon the time of the year and the position with respect to the mixed layer depth. A seasonal increase in storminess is correlated with an increase in intermittency of the turbulence in the mixed layer.
- We observed a quadratic relation between kurtosis and skewness for the statistics of ϵ.
- A co-location of patches of higher ϵ with the shear maxima of the two first baroclinic modes suggests internal waves activity plays a role in the setting the mixing intensity despite the lack of tidal forcing.
- The low-passed microstructure shear distribution seems to support this hypothesis despite possible signal contaminations.
- The variability of the stratification is ruled by several physical processes, including freshwater inputs from land, whose importance varies with the seasons; this succession has to be considered when studying the impact of climate change upon the stratification.

Corresponding author: Florian Kokoszka, `florian.kokoszka@szn.it`

Abstract

A dissection of the physics of the seasonal cycle of the oceanic upper layer stratification is necessary to improve climate predictions and to constrain the response of biogeochemical cycles to the climate change. Here we present a time series of vertical profiles of ϵ, the dissipation rate of turbulent kinetic energy, obtained from a microstructure profiler at a mid-latitude 75m-deep coastal site covering the destratification occurring during the the summer-to-winter. The main signature of the destratification is a progressive deepening of the mixed layer depth (MLD) from September to November, that finally extended to the bottom of the full water-column at the beginning of winter. By grouping the data into temporal and vertical bins we found that the statistics of ϵ depend upon the time of the year and the position with respect to the MLD. A seasonal increase in storminess is correlated with the increase in intermittency of the turbulence in the mixed layer. A co-location of patches of higher ϵ with the shear maxima of the two first baroclinic modes suggests internal waves activity plays a role in the setting the mixing intensity in the interior despite the lack of tidal forcing. The low-passed microstructure shear distribution seems to support this hypothesis despite possible signal contaminations. The actual origin of these energetic motions remains to be investigated. Overall, this study confirms that the variability of the stratification is ruled by several physical processes whose importance varies with the seasons. Predicting a change in stratification thus requires tackling the challenge of understanding and parameterising these processes.

Plain Language Summary

Numerical models predict that a major impact of climate change on the oceans will be an augmentation in the intensity of the subsurface stratification, that is, of the rapid increase in water density with depth that characterises the oceanic upper layer. This vertical gradient regulates several oceanic processes such as the stability of oceanic current, the vertical supply of nutrients to the surface and thus the carbon sequestration and the primary production. The intensity of the stratification is regulated by several processes such as the exchange of heat and freshwater with the atmosphere and mixing due to turbulence. The sources of turbulence are often highly intermittent in time in the case of storms and can be remote when generated by tides for instance. In the latter case turbulence is induced locally by the breaking of vertical oscillations of the interior layers that propagate from the remote source. Finally the intensity of each process strongly varies with the seasons. Therefore a change in the mean stratification can be due to several factors, including a different co-occurrence during the year, and disentangling them is thus crucial to have reliable predictions. Our understanding of the seasonal cycle of the turbulence is limited due to a lack of time series, a limitation that, in turn, is due to the difficulties associated to the sampling. Here we present a new time series that describes the change in stratification evolving from the highly stratified summer conditions to the vertical homogeneous winter status at a coastal site in the Mediterranean Sea. Overall we found that the turbulence characteristics vary with depth and timing over the seasons together with the change of the layer structure of the water column. We have also found the signature of intense mixing events occurring below the homogeneous layer that could be related to a recently proposed mechanism, that is, the excitation and propagation of internal oscillations that originates from a reflection of storm-driven surface horizontal oscillations by the adjacent coast. Overall, our study confirms the complexity of the interplay of the processes regulating the stratification and the urgent need of long, purposely designed time series.

1 Introduction

The stratification of the oceans, that is, the density change with depth, regulates the physical processes taking place from the surface to the bottom (Garrett et al. [1978],

de Boyer Montégut et al. [2004]). Its vertical structure, related to the vertical structure of temperature and salinity, results from the transfer of energy of large-scales forcings (e.g., winds, sea-air and ice-air buoyancy exchanges, tides) toward small dissipative scales (Wunsch & Ferrari [2004], Thorpe [2005]).

The transfer of energy occurs via a large variety of phenomena (e.g., internal waves, eddies, filaments, overturns Ferrari & Wunsch [2009]), whose roles are not perfectly disentangled. In addition, forcing sources may be remote. These different processes are regulated by the stratification which, in turn, is modified through the microscale mixing they ultimately provide (Brainerd & Gregg [1995],Mackinnon & Gregg [2005]). As discussed in Somavilla et al. [2017], the link between surface forcing and stratification is made more complex by the preconditioning role that surface forcing have on the permanent pycnocline. In a context of data analyses (Guancheng et al. [2020]) and projections that indicate that global warming leads to stronger stratification (Skliris et al. [2014], Hegerl et al. [2015], Zika et al. [2015], Pastor et al. [2018]), it is of importance to identify which processes that regulate the stratification are the most sensitive to changes.

More generally, the relative importance of specific physical processes acting on the vertical distribution of temperature and salinity strongly varies during the year, leading to an important seasonality of the interplay of fine-scale processes over the vertical dimension (Brody et al. [2014]). The seasonal conditioning of the water column stratification regulates also the biological activity since it controls the vertical transfer and uptakes of nutrients (Sverdrup [1953], Kiørboe & Mackenzie [1995]), while several marine species take advantage or are limited by the water motions modulated by the stratification (Mann & Lazier [1996], Prairie et al. [2012], Barton et al. [2014], Wheeler et al. [2019]). Understanding its seasonality is thus relevant for the biogeochemicals cycles, harmful algae blooms and plastic dispersal, among others (Sverdrup [1953], Pingree et al. [1976], Wihsgotta et al. [2019]).

Fine-scale and micro-scale observations through dedicated high resolution profilers have multiplied since the first designs of microstructure probes in the 1960's (Osborn [1998], Lueck et al. [2002], Shang et al. [2016]) to better understand how energy transfers toward small scales (in the ocean). But the difficulty of the deployment at sea and the complexity of the physical phenomena to be sampled make an in situ characterization challenging. Thus, an effort toward the acquisition of high quality data at all scales, from the open ocean to the coastal area, remains a primer. Additionally, once acquired the data interpretation remains difficult since it is not always possible to disentangle the role of single processes as pointed also by the recent study of Lozovatsky et al. [2017].

Here we present a unique attempt to describe the seasonal cycle of the vertical stratification and associated mixing with high-resolution data collected from July 2015 to February 2016. These observations contribute to the Long Term Ecosystem Research Marechiara (LTER-MC) initiative that produced a historical time series of a Mediterranean coastal ecosystem through a weekly sampling of the water column started in 1984 and running until now (Ribera d'Alcala et al. [2004], Zingone et al. [2019]). The sampling site is located on the inner shelf of the Gulf of Naples, a mid-latitude gulf in the Western Mediterrean Sea having subtropical regime and almost no tides (**Fig. 1**). The shallow semi-enclosed basin presents a marked salinity contrast due to the combination of the salty Tyrrhenian Sea waters, entering from on its southern side, with the freshwater inputs from a densely inhabited coastal area on its northern part and from nearby rivers (Cianelli et al. [2012], Cianelli et al. [2017]). Forced also by recurrent, highly seasonal intense wind forcing events, its cross-shore exchanges are modulated by mesoscale eddies and sub-mesoscale filaments (Iermano et al. [2012]). The important role of lateral transport of freshwater in setting the stratification implies also that long term changes are possibly impacted also by the effects of climate change on the surrounding territories, which include regions with important winter snow accumulations. Thus, the study area is an ideal site to study how coastal salinity and temperature changes combine in setting the variability of the

133 vertical stratification (Woodson [2018]), in a context of rising air and sea temperatures
134 and of intensifying extreme events such as storms, floods and even, recently, Mediter-
135 ranean hurricanes (Volosciuk et al. [2016], Koseki et al. [2020], W. Zhang et al. [2020]).

136   For this purpose, we will present first the hydrology obtained from the Conductiv-
137 ity–Temperature–Depth (CTD) measurements to depict the vertical structure of the water-
138 column during the seasonal cycle at the coastal area. To identify the drivers of the de-
139 stratification during the seasonal cycle, we will then investigate the timing and inten-
140 sity of wind stress and buoyancy fluxes during the course of the mixed layer depth deep-
141 ening weeks after weeks. Internal layers susceptible to intermittent diffusive convection
142 and double diffusion regimes will be investigated as they may be impacted by changes
143 in vertical stability due to surface forcings. We will describe then the occurrence of a bot-
144 tom turbid layer. Finally, we will present the seasonal cycle of the turbulent kinetic en-
145 ergy dissipation rates obtained from vertical microstructure profiles, and describe their
146 characteristics following the statistical framework of Lozovatsky et al. [2017]. We will
147 conclude by depicting a conceptual scheme that illustrates the processes possibly at work
148 during the summer-to-winter transition.

2 Materials and Methods

2.1 Hydrology and mixed layer depth (MLD)

151   Conductivity–Temperature–Depth (CTD) profiles were carried out at the LTER-
152 MC sampling point in the Gulf of Naples (**Fig. 1**) with a Seabird `SBE-911+` mounted
153 on a 12-bottle carousel, with all sensors calibrated. The raw 24 Hz profiles were processed
154 using the Seabird data processing SeaSave 7.26.7 to obtain 1-m bin-averaged data. The
155 weekly survey refers to the casts MC1160 to MC1190 and includes a total of 31 CTD
156 profiles (supplementary Tab. S1). Independent to these data, the vertical microstruc-
157 ture profiler (`VMP-250` from Rockland Scientific International Inc, henceforth reffered to
158 as Rockland) used in this study was equipped with a nose-mounted high-precision conductivity-
159 temperature sensors (micro-CT) from JFE Advantech, sampling at 64 Hz. These data
160 were averaged on a regular vertical grid of 10 cm, and allowed us to collect a second hy-
161 drological dataset, directly co-located with the microstructure measurements. CTD data
162 were used to provide a general view on the hydrological context of our study (periods
163 of external forcings, mixed layer depth, vertical internal layers of the water-column), and
164 micro-CT data to infer the Turner's regimes (see Section 2.2). For both datasets, the Gibbs-
165 SeaWater Oceanographic Toolbox (McDougall & Barker [2011]) was used to calculate
166 the conservative temperature T_C (°C), the absolute salinity S_A (g kg^{-1}), the water den-
167 sity ρ (kg m^{-3}), the potential density σ_0 (kg m^{-3}), the potential temperature θ_0 (°C),
168 and the Brunt-Väisälä frequency N^2 (s^{-2}). When mentioned thereafter, T and S refer
169 to T_C and S_A. Mixed layer depth (MLD, m) was calculated following the method of de
170 Boyer Montégut et al. [2004] based on threshold values. Given a vertical profile of den-
171 sity $\sigma_0(z)$, or potential temperature $\theta_0(z)$, we calculated the depth below $z_{ref} = 3\ m$,
172 where the profile reached thresholds defined as a cumulative of 0.4°C for θ_0, and 0.03 $kg\ m^{-3}$
173 for σ_0. The VMP was also equipped with a fluorometer-turbidity sensor from JFE Ad-
174 vantech, sampling at 512 Hz. These data were converted to physical units using the ODAS
175 Matlab Toolbox provided by Rockland (version 4.4.06). The sensor has a spatial response
176 of ~ 1 cm (Wolk et al. [2002]) and the data were averaged over 10 cm. A mean value of
177 -2.5 FTU over the whole cast was taken as a reference to establish a ΔFTU and iden-
178 tify turbid layers in the water-column.

2.2 Turner's regimes

180   We applied the method introduced by Turner (Turner [1967], [1973]) to localize parts
181 of the water column where vertical gradients of T and S are favourable to double-diffusive
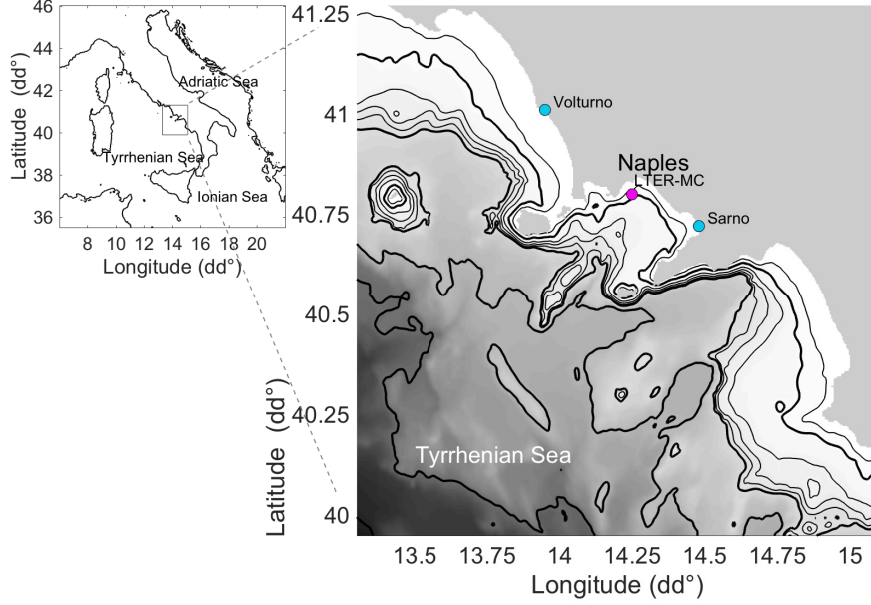182 instability. The high-resolution CT data from the JFE Advantech sensor mounted on

Figure 1: Bathymetry of the Gulf of Naples (GEBCO grid [GEBCO, 2020]) along the Tyrrhenian Sea in the Mediterranean basin). The 75m-deep LTER-MC coastal sampling site $(14.25°E, 40.80°N)$ is located by the pink dot. Volturno and Sarno's river mouths are shown in blue. Thin lines indicate the 50, 200, 300 and 400 m isobaths, thick ones indicate the 100, 500, 1000 and 2000 m isobaths.

the `VMP-250` was used for this analysis. Combining the vertical gradients and their signs allows the identification of stability regimes, that can be defined from the ratio $R_\rho = (\alpha d\theta/dz)/(\beta dS/dz)$ where $\alpha = -\rho^{-1}(d\rho/d\theta)$ is the thermal expansion coefficient, $\beta = \rho^{-1}(d\rho/dS)$ is the haline contraction coefficient, where $d\rho/dz$ and $d\theta/dz$ are the vertical gradients of density and temperature, respectively. This ratio is used to calculate the Turner angles (°) $Tu = \arctan((1+R_\rho)/(1-R_\rho))$ (Ruddick [1983]). The value of the Turner angle defines various stability regimes. A diffusive convection regime (e.g., fresh cold layers over warm salty layer) arises when $-90° < Tu < -45°$. A double-diffusive regime (e.g., salty warm layer over cold fresh layer) arises when $45° < Tu < 90°$. Within each of these regimes, the instability is higher when $|Tu|$ is close to 90 degrees. A stable regime occurs when $|Tu| < 45°$, whereas a gravitationally unstable regime occurs when $|Tu| > 90°$.

2.3 Heat fluxes, winds and precipitations

Surface heat fluxes (latent and sensible, with net solar and thermal radiation, in $W\,m^{-2}$), wind velocities (U_{10} and V_{10}, $m\,s^{-1}$), evaporation E and precipitation rates P ($mm\,d^{-1}$) were extracted from the ERA5 re-analysed product provided by Copernicus (ERA5(C3S) [2017]). The closest grid-point was selected from the LTER-MC geographical position ($14.25°E$ and $40.80°N$), with a 6-hour temporal resolution, over the whole period. We used those values to infer the Monin-Obukhov length scale (L_{MO}) (Obukhov [n.d.], Obukhov [1971]), a critical length scale describing the depth at which the turbulence is generated more by wind shear than buoyancy forcings, defined as $L_{MO} = u_*^3/\kappa B$ (m). Here u_* is the friction velocity of the wind ($m\,s^{-1}$), κ the von Karman's constant (here 0.4), and B the buoyancy flux ($m^2\,s^{-3}$), defined such that $B > 0$ if stabilizing the

water-column. Buoyancy flux is proportional to the density flux at the surface, as $B = gQ_p/\rho_0$, where the density flux Q_p into the ocean from the atmosphere was computed as (H.-M. Zhang & Talley [1998]) $Q_p = \rho(\alpha F_T + \beta F_S)$, with α and β the thermal expansion and saline contraction coefficients, respectively. Here $F_T = -Q_{net}/\rho_{sea}C_p$, and $F_S = (E - P)S/(1 - S/1000)$, where C_p is the specific heat of sea water, E, P, and S are the evaporation, precipitation and sea surface salinity. The net radiative heat flux at the ocean surface Q_{net} (W m^{-2}) was calculated from the combination of the incoming short wave, net incoming and emitted long wave, sensible and latent heat. The velocity friction u_* was calculated as $u_* = \sqrt{\tau/\rho_{sea}}$, where ρ_{sea} is the density of sea water, and τ the wind stress, as $\tau = \rho_{air}C_D U_{10}^2$, where $\rho_{air} = 1.22$ kg m^{-3}, and drag coefficient C_D and velocity at 10 m U_{10} calculated from wind velocity following Large & Pond [1981]. Different regimes can be identified from the L_{MO} diagnostic : wind stress dominance over stable B ($L_{MO} > 1$), stable B dominating the wind stress ($0 < L_{MO} < 1$), wind stress dominating a destabilising B ($L_{MO} < -1$), and a destabilising B dominating wind stress ($-1 < L_{MO} < 0$).

2.4 Microstructure data

Microstructure measurements were collected at the LTER-MC point using a `VMP-250` profiler from Rockland. During each deployment, between one and four profiles were completed down to five meters above the bottom (75 m deep), resulting in a total of 71 profiles among the 31 weekly CTD profiles of the survey (supplementary Tab. S1). The profiler was deployed with a tether from the ship and fell quasi-freely at a speed of 0.7 m s^{-1} to 0.9 m s^{-1}. The profiler was equipped with two microstructure shear sensors, a fast response temperature sensor (FP07) and a micro-conductivity sensor (SBE7), which were all sampled at 512 Hz. The shear probes measured the vertical shear of horizontal velocity fluctuations (i.e. du/dz, dv/dz). The raw signals are subject to noise and signal contamination from instrument vibrations, internal circuitry, and impact of biology and sediment. To reduce the impact of signal contamination, several processing steps were required before computing the spectra and dissipation rate. Firstly, the upper and lower meters of each cast, where the profiler was accelerating and decelerating, were discarded. These segments were identified and removed manually when the profiling speed deviated from the median value by more than ± 1.5 times the standard deviation. Secondly, large amplitude, short-duration spikes were eliminated from the shear data using the despiking algorithm provided in Rockland's ODAS Matlab Library (v4.4.06). In particular, spikes were identified using a threshold value of 5 when comparing the instantaneous shear signal to a smoothed version. The smoothed signal was obtained using a first-order Butterworth filter, with a cut-off frequency ranging from 0.7 to 0.9 Hz, depending on the median value of the fall speed. Once identified, spikes were removed over a 5 cm segment (ca. 0.07 s). Thirdly, the shear signals were high-pass filtered at 1.5 Hz to remove low-frequency contamination (0.1 - 1 Hz) that is believed to be associated with the pyroelectric effect. The spectrum of the high-passed vertical shear signal was computed and used to estimate the dissipation rate (see below). The low-frequency portion of the signal, i.e. Sh_{LP}, from shear probe 1 was also analyzed (see Appendix).

2.5 Dissipation rate

The dissipation rate of turbulent kinetic energy (TKE) was calculated using the isotropic relation $\epsilon = 7.5\nu\langle(\frac{\partial u}{\partial z})^2\rangle = 7.5\nu\langle(\frac{\partial v}{\partial z})^2\rangle$, where ν is the kinematic viscosity of seawater and u and v are the horizontal components of the small-scale velocity fluctuations. In practice, the estimate of ϵ was obtained iteratively by integrating the shear spectra up to an upper wavenumber limit ($k_{\max}$), i.e. $\epsilon = 7.5\nu\int_0^{k_{\max}}\phi(k)dk$ as is outlined in Rockland's Technical Note 028 (Lueck [2016]). This was done for each microstructure sensor separately, i. e. for du/dz (as sh_1) and dv/dz (as sh_2). The shear spectra, and hence dissipation rates, were estimated using the ODAS Matlab Library (v4.4.06).

Dissipation segment lengths of 3 s were used with 1 s fft-segments that overlapped by 50%. The dissipation segments themselves were overlapped by ca. 1.5 s, which resulted in a vertical resolution in ϵ of approximately 1.2 m. Contamination of the spectra for instrument vibrations was reduced using the cross-coherency method of Goodman et al. [2006]. The quality of the spectra were assessed using a figure of merit, which is defined as $FM = \sqrt{dof} \times mad$, where $dof = 9.5$ is the number of degrees of freedom of the spectra (Nuttall [1971]) and mad is the mean absolute deviation of the spectral values from the Nasmyth spectrum as $mad = \frac{1}{n_k} \sum_{i=1}^{n_k} |\frac{\phi(k_i)}{\phi_{\text{Nasmyth}}(k_i)} - 1|$ where n_k is the number of discrete wavenumbers up to $k_{\max}$ (Ruddick et al. [2000]). Segments of data where the spectra had $FM > 1.5$ were rejected from further analysis. The final dissipation rate was obtained by averaging the estimates for the two independent probes, i.e. ϵ_1 and ϵ_2 (respectively from sh_1 and sh_2). If the values of ϵ_1 and ϵ_2 differed by more than a factor of 10, the minimum value was used. FM values and Nasmyth's fit are included in the Fig. S1 of the Supplementary information. Probability distribution functions (pdfs) of ϵ were computed with the Matlab Statistical Toolbox. Pdfs were obtained over various temporal and depth bins covering the physical domain of external forcings and vertical layers.

3 Results

3.1 Hydrology from the CTD profiles

The Gulf of Naples (**Fig. 1**) stands as a non-tidal coastal area in the Western Mediterranean marked by a subtropical regime, and is directly affected by continental freshwater runoffs and salty water from the Tyrrhenian Sea.

We present on **Fig. 2.a** the hydrology of the water-column during our survey. A clear seasonal cycle is visible : a stratified period in July-August, followed by a progressive deepening of the MLD from September to November, that finally reaches a period when the water-column can be considered as fully mixed, from December to February. From the surface down to 50-60 m depth, relatively fresh waters persist all along the summer till early November after which they are rapidly replaced by salty waters that remain till the end of the record (**Fig. 2.a**).

A salty bottom layer of 38.1 to 38.3 g kg^{-1} is visible below the 28.3 kg m^{-3} isopycnal layer all along the record. As for the general pattern of the Brunt-Väisälä frequency N^2 (**Fig. 2.b**), a strongly stratified, 10 m thick transitional layer is observed below the MLD, separating the surface from the internal and bottom layers (Johnston & Rudnick [2009]). To identify the physical processes acting below the MLD, we partitioned the column into layers using a vertical decomposition into baroclinic modes 1 and 2 (see Supplementary information S2), denoted by B1 and B2 respectively. The determination of their vertical extension was made for each profile by identifying the depth ranges containing the shear maximum values. The maxima of B1 are located immediately below the MLD and are associated with the highly stratified part of the water column, while the maxima of B2 lie deeper and are associated with a weaker stratification (see supplementary Fig. S2). Finally, the water column between B2 and the bottom was considered as a separate layer. We present the vertical extension of the vertical bins in **Fig. 2.c**. This partitioning was then used for the statistical characterization of the destratification.

3.2 Buoyancy fluxes and wind forcings

The time evolution of buoyancy fluxes and surface winds is investigated to look for possible impacts on the deepening of the MLD. In general, positive buoyancy fluxes strengthened the stratification of the water column while negative buoyancy fluxes weaken the stratification and may lead to surface convection and deepening of the MLD. During summer and till mid-September, the daily averaged B was always positive apart from three
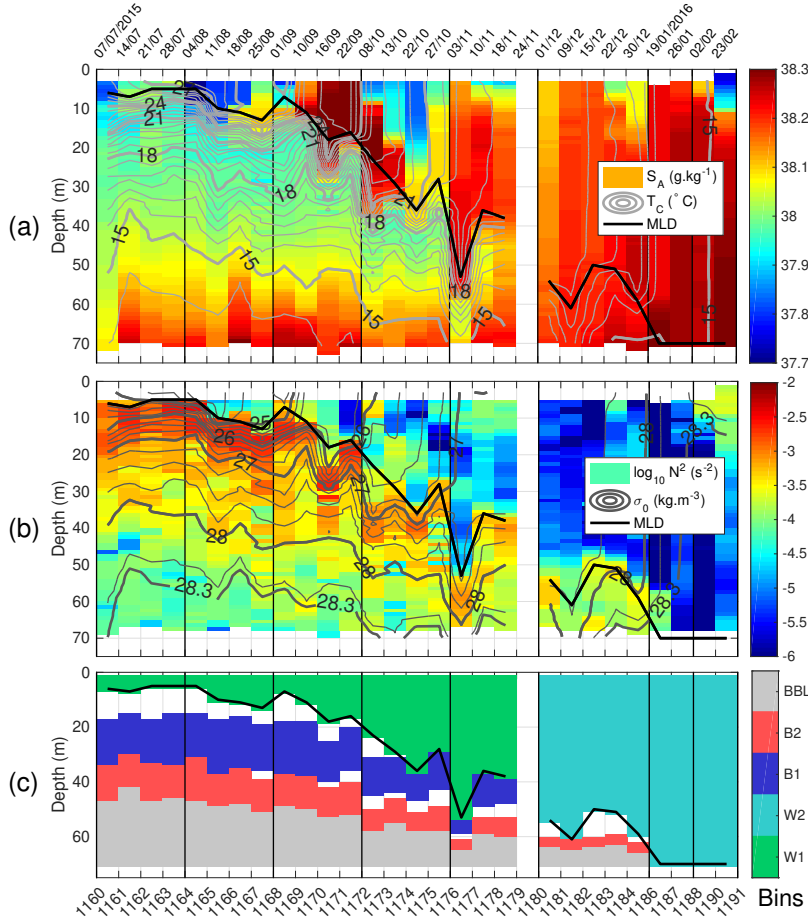
Figure 2: CTD `SBE-911+` profiles. (a) Absolute Salinity S_A (g kg^{-1}) with contours of Conservative temperature T_C (°C). (b) Brunt-Väisälä frequency N^2 (s^{-2}) and contours of potential density σ_0, plotted from 24 to 27 kg m^{-3} every 0.25 kg m^{-3}, with the 28.3 kg m^{-3} isopycnal emphasized in thick black near the bottom. (c) Vertical and temporal bins used thereafter for the statistical characterization by periods and layers : surface to MLD during the summer to autumn period $W1$ (green), surface to MLD during the winter period $W2$ (cyan), the vertical layer of the shear maxima of the first baroclinic mode $B1$ (blue) and second baroclinic mode $B2$ (red), and the bottom boundary layer BBL (gray). (All) $MLD_{\theta_0}^{0.4°C}$ (thick black line). X-axis indicates the sequence of MC-CTD profiles references, and sampling dates are given on the panel top.

short episodes of negatively buoyant days (**Fig. 3.a**, gray line). In contrast, after mid-September B remained negative (or close to zero). Consequently, from the beginning of the observed period, the cumulative buoyancy flux increases and reaches a maximum level around mid-September and then constantly decreases from mid-October to reach a minimum at the end of the record (**Fig. 3.a**, gray dashed line). The contribution of heat (B_T) and freshwater (B_S) fluxes to daily buoyancy fluxes clearly show that B_T dominates, being larger than B_S by one order of magnitude except during rain events (**Fig. 3.a** and **Fig. 3.b**, blue lines). Precipitation rates shows intermittent events with values larger than 20 mm d^{-1}, with a maximum of about 70 mm d^{-1} in early October, followed by intermittent rainy events during the rest of the period. During those events, (positive) B_S became comparable to B_T (**Fig. 3.a**, solid pink blue and gray lines). Note that without measurements of the river runoffs contribution, there were not accounted

for despite they are likely of importance over this coastal area (the Sarno river runoff into the Gulf of Naples is about 13 m^3 s^{-1}, while the Volturno river runoff into the Gulf of Gaeta is about 82 m^3 s^{-1} (Albanese et al. [2012])).
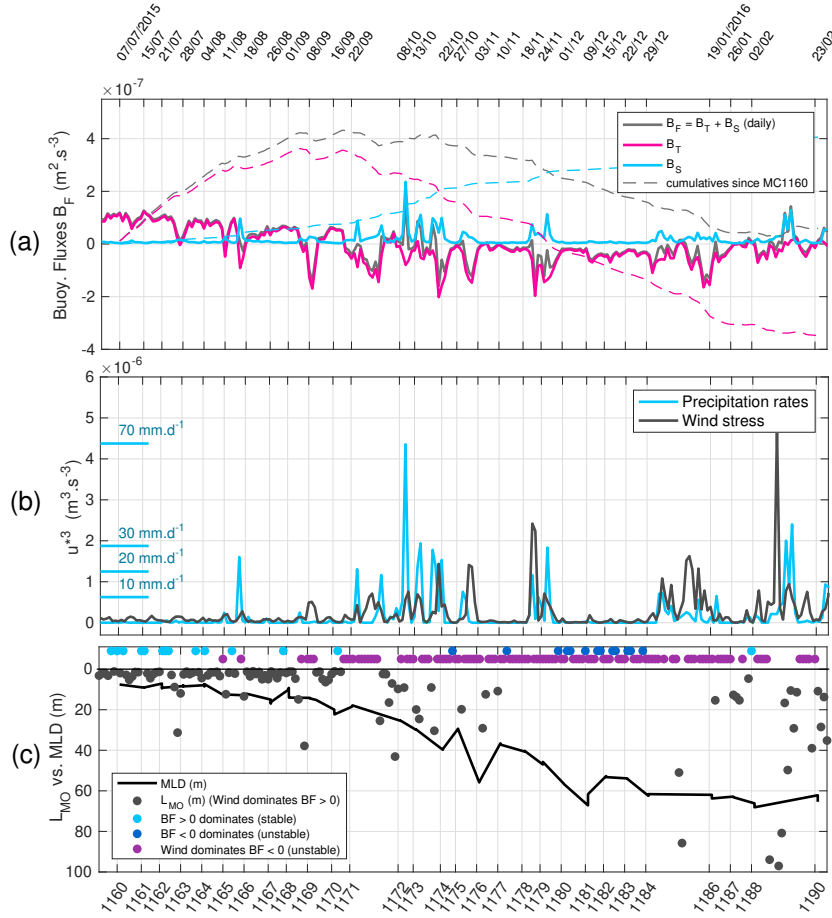

Figure 3: (a) Daily averaged buoyancy fluxes B (m^2 s^{-3}). Gray line indicates the sum of heat and freshwater contributions B_T (solid pink) and B_S (solid blue). The associated dashed lines indicate the cumulative values from the 7th of July 2015 (scaled down by a factor 10 for graphical purposes). (b) Daily averaged precipitation rates P (mm d^{-1} in blue) and wind stress u_*^3 (m^3 s^{-3} in gray). (c) MLD (solid black) and Monin-Obhukov length scale L_{MO} (m in gray dots) during stable buoyancy fluxes. On the horizontal line near surface, dots indicate the occurences of the other regimes (stable in light blue, unstable dominated by negative fluxes in dark blue, and unstable fluxes dominated by wind stress in purple). X-axis indicates the MC-CTD casts references. Sampling dates are given on the panel top.

Buoyancy fluxes counteract the wind stresses, which are able to mechanically mix the surface layer and contribute to the deepening of the MLD. The wind stress (**Fig. 3.b**) over the summer period is weak and shows few intermittent events before the mid-September (MC1171) with $u_*^3 < 0.5 \times 10^{-6}$ m^3 s^{-3}. Stronger energetic storms with values $> 1.5 \times 10^{-6}$ m^3 s^{-3} occurred two months later, around the 20th November, followed in January and February by other stormy periods. To identify the direct contribution of the wind to the mixing within the water column, we calculated the Monin-Obhukov length scale (see Methods) to characterize the dominance of wind stress over positive buoyancy fluxes. Unre-

alistically large values (i.e. $|L_{MO}| > 100$ m) have been discarded. Note that, because strong winds prevented any ship observation during storms, the MLD was only diagnosed after (and not during) the occurrence of extreme events, inhibiting a detailed analysis of covariance between MLD and L_{MO} during stormy periods.

We show on **Fig. 3.c** (gray dots) cases when wind mechanical forcing was responsible for the MLD deepening. During the stratified period, the L_{MO} remained in the range of $0.01 - 1$m, that is, the winds were too weak to break the stratification and thus to deepen the MLD (MC1160 to MC1170 included, from July to mid-September). Strong values of $u_*^3 > 0.5 \times 10^{-6}$ m^3 s^{-3} occurred after MC1171, after which the L_{MO} regime shifted toward values $O(10\,m)$ until MC1177 included (mid-November). The strong event of $u_*^3 > 2 \times 10^{-6}$ m^3 s^{-3} of the end of November between MC1178 and MC1179 marked the start of the winter period, with values of L_{MO} reaching values $> 10\,m$ between MC1184-MC1186 and MC1188-MC1190. Most of the MLD deepening occurs during the period from late-summer to winter. Despite this period is characterized by negative buoyancy fluxe, our analysis cleary shows that wind forcings dominates over B (**Fig. 3.c**, purple points) rather than the opposite (dark blue dots). Thus, the MLD deepening is mostly induced by wind mechanical mixing. Cases with no significant wind conditions occurred mainly in December, with some additional short events in October and November.

This change of the main atmospheric forcings properties over the seasons led us to split the analysis of two temporal periods : $W1$ from MC1160 to MC1178 (July to mid-November), and $W2$ from MC1179 to MC1190 (end of November to February), respectively (**Fig. 2.c**).

3.3 Turner's regimes : diffusive convection and double diffusion

The seasonal variability we observed is associated with large variations of the thermohaline vertical gradients that may drive various regimes of stability. We quantify those different regimes through the study of Turner's angles, estimated from the relative contribution of vertical gradients of salinity and temperature (Section 2.2). There is a clear partition of the stability between diffusive convection and salt fingering regimes at the MLD (**Fig. 4.a**). In the fall and winter months, the diffusive convection regime occupies the region above the MLD, whereas in the summer months the salt-fingering regime is present beneath the ML. More complete statistics of the Turner angles are presented in supplementary Tab. S2. Diffusive convection regime is observed locally with patchy structures that appeared in August at the surface, followed by larger ones in October, between 10 and 30 m . This situation repeated in December, although the vertical distribution of this regime is more variable. Below the ML, a pattern of double diffusive regime is visible, driven by warm and salty water overlaying on the relatively colder and cooler layers. The period from mid-September to November presented layers prone to salt-fingering that were located below the local maximum of salinity of $38.2\,g\,kg^{-1}$. The periods $W1$ (late summer and fall) and $W2$ (winter) presented differences in the intensity of the diffusive regime, with median intensity of $Tu \approx -45°$ and $R_\rho \approx 0.33$ during $W1$, weaker in term of instability than for $W2$ showing median values $Tu \approx -72°$ and $R_\rho \approx 0.5$. In terms of salt fingers, the regime observed in the ML during the destratification shows a median value of $Tu \approx 59°$ and $R_\rho \approx 3.8$, which is more intense than the regime found below the MLD (median $Tu \approx 50°$ and $R_\rho \approx 8.4$).

3.4 Turbidity observations

The seasonal variability of vertical mixing is associated here with some patterns visible in the turbidity measurements of the JFE Advantech Co. fluorometer-turbidity sensor mounted on the `VMP-250` (**Fig. 4.b**). These data indicate a turbid bottom layer co-located with the deep salty layer (**Fig. 2.a**). When the ML reaches the proximity of the bottom, from the end of October to December, some turbid bottom patches are vis-
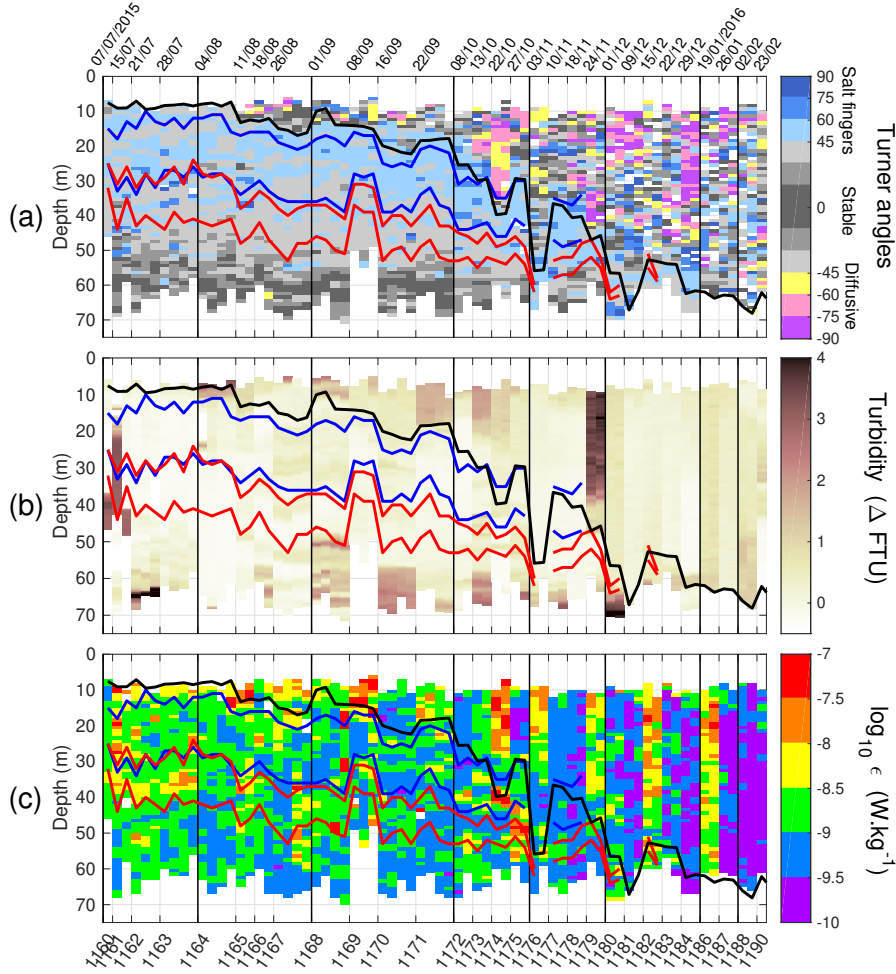
Figure 4: `VMP-250` profiles, plotted sequentially (x-axis does not represent time). (a) Turner angles (angular °), (b) Turbidity (ΔFTU) (offset from a reference value), and (c) Dissipation rate estimates (W kg^{-1}). (All) $MLD_{\theta_0}^{0.4°C}$ (thick black), region of maximum energy of baroclinic mode 1 (between blue lines) and mode 2 (between red lines). The VMP profiles are plotted sequentially along the x-axis, where the MC casts references are indicated (from one to four VMP profiles by cast). Sampling dates are given on the panel top.

379   ible (MC1175 on the supplementary Fig. S3.b, or MC1180 on Fig. S3.c). This provides
380   evidence of the re-suspension of sediments in a non-tidal area, by energetic processes lo-
381   cated between the MLD and the bottom boundary layer. Once a full vertical homoge-
382   nization is achieved in January (the core of winter period), no additional turbid layers
383   are observed. Looking at the subsurface, local turbid patches are present inside the ML
384   from September to November, with structures occupying a large part of the water col-
385   umn (MC1179 on **Fig. 4.b**). This depicts the complexity of the winter mixing at the
386   coastal area, underlying the possible important role of the runoffs discharging sediments
387   at various point of the coast, and of the mesoscale and submesoscale features laterally
388   advecting them.

3.5 Turbulent kinetic energy dissipation rate ϵ

The seasonal sequence of vertical profiles of dissipation rates of turbulent kinetic energy shows maximum values between 10^{-8} and 10^{-7} W kg^{-1} (**Fig. 4.c**), distributed through patches in various parts of the water column. For a given station, ϵ varies within a factor of five between the successive casts done typically within one hour (e.g., stations MC1163, MC1168, or MC1171). The summer period shows values of 10^{-8} W kg^{-1} at the depth-range of the MLD, around 10 m. The most intense patches are from 5×10^{-7} to 10^{-8} W kg^{-1} between 20 and 35 m in July (MC1160 to MC1163), then between 35 and 50 m in August and September (MC1164 to MC1171). They match the MLD depth in October (MC1174 and MC1175). Minimum values of 10^{-10} W kg^{-1} are measured, which are near the noise limit of the instrument. In winter, the dissipation rates are low throughout most of the water column (MC1184, MC1188, MC1190). The turbid patches identified previously are associated with local patches of ϵ from August to January, with values from 10^{-8} to 10^{-7} W kg^{-1} in surface from 10 m to around 20 m (MC1165, MC1171, MC1174), and in the lower range of around 10^{-9} to 10^{-8} W kg^{-1}, into the water column (MC1179, MC1186) or at the proximity of the bottom (MC1168, MC1173).

Profiles of ϵ are grouped by their mean and median values over the stratified period $W1$ and winter period $W2$ (**Fig. 5**). During $W1$, the median profiles converge from 10^{-8} to 10^{-9} W kg^{-1} from 10 to 25 m, and then remains around 10^{-9} W kg^{-1} down to the bottom, punctuated by local intense values $> 10^{-7}$ W kg^{-1}. Layers below the ML show intermittent local maximum values reaching 10^{-8} W kg^{-1}, located in the vertical between region of the two first baroclinic modes maximum. The winter period $W2$ shows a tendency of $\langle\epsilon\rangle$ values to be centered around 10^{-10} and 5×10^{-8} W kg^{-1} (**Fig. 5.b**). Peaks are observed at various depths in the water-column, marking both spatial and temporal intermittency. They are more pronounced in the stratified layers, which may underline that intermittency is stronger in these locations. It should be noted that our observations were made when weather conditions were favourable for a safe deployment of the `VMP-250`, sometimes after energetic storms but certainly never during storms. Therefore, the most intense turbulent events are likely missed.

3.6 Statistical description of ϵ and N^2

To characterize the distributions of ϵ, we applied the same framework as Lozovatsky et al. [2017]. We present in **Fig. 6** the empirical probability density function (pdf) of ϵ and N^2 on the two forcing periods W1 and W2, and differentiate the surface from the internal and bottom layers B1, B2 and BBL (see **Fig. 2.c**).

3.6.0.1 Pdf of ϵ and N^2 The pdf for the surface bins (**Fig. 6.a**) shows values around 4×10^{-10} W kg^{-1} for W1, and 2×10^{-10} W kg^{-1} for W2, the latter being dominated by stronger winds and negative buoyancy fluxes. Both distribution are well fitted by a Burr type XII, and differ from log-normality. Regarding the stratification (**Fig. 6.b**), the summer to fall period shows a distribution centered on 5×10^{-5} s^{-2} (W1 in green), while winter is characterized by a distribution centered on 3×10^{-5} s^{-2} (W2 in cyan). Below the mixed layers (**Fig. 6.c**), the pdf of ϵ shows a dominant peak centered on 5×10^{-10} W kg^{-1} for B1, and on 9×10^{-10} W kg^{-1} for B2. The distribution within the BBL (**Fig. 6.e**) is narrower compared to B1 and B2, and shows a dominant peak centered on 7×10^{-10} W kg^{-1}. The observations are better described by the Burr type XII distribution than the log-normal, even if the deviation from log-normality is not so pronounced than for the distributions of the surface bins W1 and W2. Regarding the N^2 below the ML (**Fig. 6.d**), the pdf in B1 is centered around 4×10^{-4} s^{-2} and close to log-normality. The distribution in B2 is more variable, with values spread in the range 2×10^{-5} to 3×10^{-4} s^{-2}, making difficult to distinguish which distribution fits better. Similarly, in the BBL (**Fig. 6.f**) values are spread in a wide range (3×10^{-5} to 2×10^{-4}
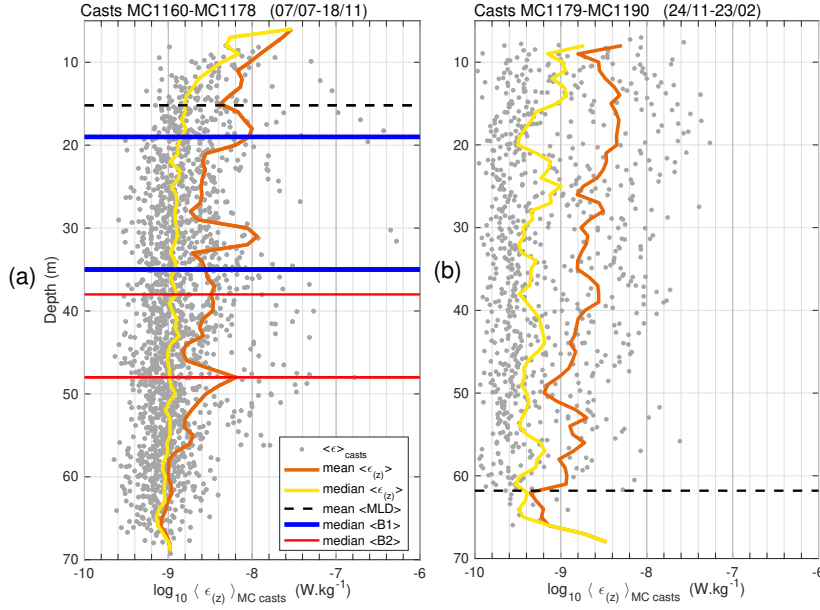
Figure 5: Mean (orange) and median (yellow) profiles of ϵ $(\mathrm{W\,kg^{-1}})$ over the (a) summer-fall period W1 and (b) winter period W2. Gray background points are individual ϵ estimates. Horizontal dashed lines indicates the median depths of the MLD (black) and the upper and lower depths of B1 (blue) and B2 (red) during the stratified period $W1$.

s^{-2}), with a central peak at 7×10^{-5} s^{-2}, making it difficult to define a best fit between Burr and log-normal distributions. Details of statistics are given in **Tab. 1.a,b**.
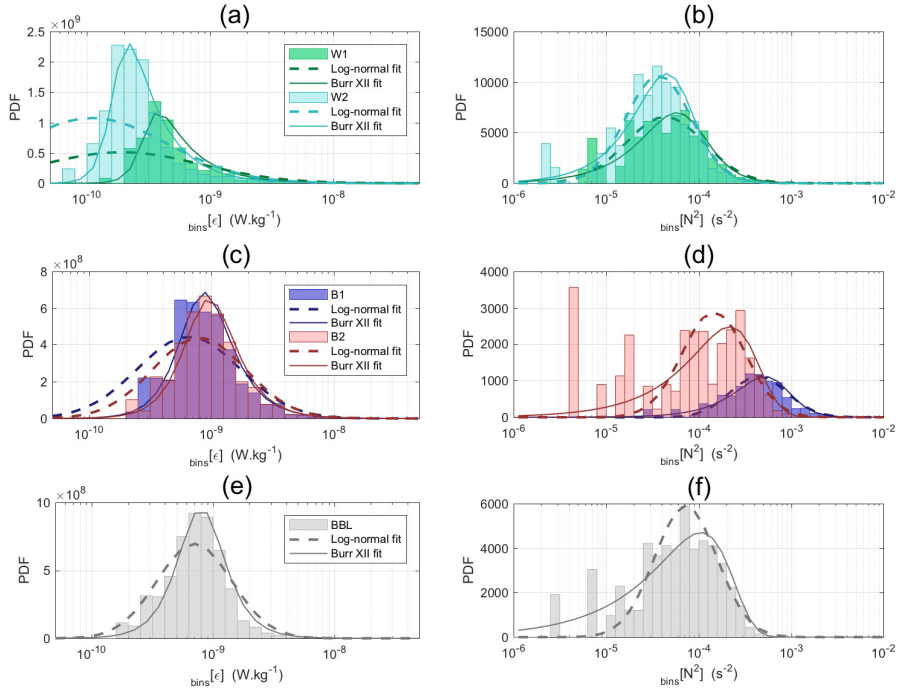
Figure 6: PDFs of ϵ (W kg^{-1}) (left), and N^2 (s^{-2}) (right), through temporal bins W1 and W2 (a,b), vertical layers B1 and B2 (c,d), and near the bottom BBL (e,f). Fits of log-normal and Burr type XII distribution are indicated with the dashed and plain black lines, respectively. Bins are shown on Fig. 2.c, and detailed statistics are given in Tab. 1.

Table 1: Statistics of ϵ (a) and N^2 (b). For both quantities are given general statistics by bins, and parameters for the fits of log-normal and Burr Type XII distributions, with their confidence intervals (c.i.). (c) Parameters of the quadratic fit $K = aS^2 + b$ of the $K = f(S)$.

(a) Statistics for ϵ

General

Bin	N (Pop.) (by bins)	Total (All data)	%	mean	median	skewness	kurtosis
W1	372	3084	12	5.70×10^{-9}	1.07×10^{-9}	5.82	51.58
W2	771	3084	25	2.38×10^{-9}	4.05×10^{-10}	4.67	31.56
B1	561	3084	18	5.23×10^{-9}	1.23×10^{-9}	12.33	162.21
B2	379	3084	12	2.95×10^{-9}	1.30×10^{-9}	13.43	217.17
BBL	638	3084	21	1.51×10^{-9}	9.63×10^{-10}	7.08	67.67

Log-normal fit

Bin	mean	median	μ	[c.i.]	σ	[c.i.]
W1	4.88×10^{-9}	1.59×10^{-9}	-20.25	$[-20.40 - -20.10]$	1.49	[1.39 - 1.61]
W2	1.90×10^{-9}	7.09×10^{-10}	-21.06	$[-21.16 - -20.96]$	1.40	[1.33 - 1.48]
B1	2.38×10^{-9}	1.48×10^{-9}	-20.32	$[-20.40 - -20.24]$	0.96	[0.91 - 1.02]
B2	2.24×10^{-9}	1.52×10^{-9}	-20.29	$[-20.38 - -20.20]$	0.87	[0.81 - 0.94]
BBL	1.33×10^{-9}	1.03×10^{-9}	-20.68	$[-20.74 - -20.63]$	0.71	[0.67 - 0.75]

Burr XII fit

Bin	mean	median	α	[c.i]	c	[c.i.]	k	[c.i.]
W1	Inf	9.47×10^{-10}	2.80×10^{-10}	$[2.54 - 3.08 \times 10^{-10}]$	7.06	[5.03 - 9.92]	0.08	[0.05 - 0.11]
W2	Inf	4.56×10^{-10}	1.60×10^{-10}	$[1.50 - 1.70 \times 10^{-10}]$	6.82	[5.57 - 8.37]	0.09	[0.07 - 0.12]
B1	4.18×10^{-9}	1.24×10^{-9}	7.19×10^{-10}	$[6.47 - 7.98 \times 10^{-10}]$	3.98	[3.35 - 4.72]	0.30	[0.23 - 0.38]
B2	3.19×10^{-9}	1.31×10^{-9}	8.09×10^{-10}	$[7.14 - 9.15 \times 10^{-10}]$	3.90	[3.21 - 4.73]	0.33	[0.25 - 0.45]
BBL	1.42×10^{-9}	9.55×10^{-10}	7.00×10^{-10}	$[6.42 - 7.63 \times 10^{-10}]$	3.99	[3.51 - 4.52]	0.46	[0.37 - 0.57]

(b) Statistics for N^2

General

Bin	N (Pop.) (by bins)	Total (All data)	%	mean	median	skewness	kurtosis
W1	552	3863	14	1.71×10^{-4}	9.66×10^{-5}	4.27	24.76
W2	990	3863	26	9.07×10^{-5}	6.35×10^{-5}	5.32	58.95
B1	733	3863	19	8.27×10^{-4}	6.40×10^{-4}	1.65	5.85
B2	544	3863	14	3.04×10^{-4}	2.74×10^{-4}	2.16	13.35
BBL	803	3863	21	1.49×10^{-4}	1.30×10^{-4}	1.01	4.24

Log-normal fit

Bin	mean	median	μ	[c.i.]	σ	[c.i.]
W1	1.61×10^{-4}	1.00×10^{-4}	-9.20	$[-9.28 - -9.12]$	0.97	[0.92 - 1.03]
W2	8.96×10^{-5}	6.41×10^{-5}	-9.65	$[-9.70 - -9.60]$	0.81	[0.78 - 0.85]
B1	8.34×10^{-4}	6.49×10^{-4}	-7.33	$[-7.39 - -7.28]$	0.70	[0.67 - 0.74]
B2	3.25×10^{-4}	2.39×10^{-4}	-8.33	$[-8.40 - -8.27]$	0.78	[0.73 - 0.83]
BBL	1.59×10^{-4}	1.17×10^{-4}	-9.04	$[-9.09 - -8.99]$	0.77	[0.74 - 0.81]

Burr XII fit

Bin	mean	median	α	[c.i.]	c	[c.i.]	k	[c.i.]
W1	1.95×10^{-4}	9.52×10^{-5}	7.52×10^{-5}	$[6.15 - 9.19 \times 10^{-5}]$	2.13	[1.86 - 2.44]	0.71	[0.54 - 0.92]
W2	9.40×10^{-5}	6.33×10^{-5}	6.02×10^{-5}	$[5.09 - 7.12 \times 10^{-5}]$	2.24	[2.03 - 2.48]	0.92	[0.72 - 1.17]
B1	8.49×10^{-4}	6.53×10^{-4}	6.89×10^{-4}	$[5.56 - 8.53 \times 10^{-4}]$	2.41	[2.12 - 2.73]	1.09	[0.79 - 1.52]
B2	3.03×10^{-4}	2.65×10^{-4}	6.91×10^{-4}	$[4.50 - 11.0 \times 10^{-4}]$	1.87	[1.69 - 2.06]	4.50	[2.46 - 8.20]
BBL	1.49×10^{-4}	1.32×10^{-4}	9.05×10^{-4}	$[2.08 - 39.1 \times 10^{-4}]$	1.69	[1.55 - 1.84]	18.24	[2.04 - 163.08]

(c) Quadratic fit parameters

	$K_\epsilon = f(S_\epsilon)$ $K = aS^2 + b$	$K_{N2} = f(S_{N2})$ $K = aS^2 + b$
Coeff. (with 95% conf. bounds)		
a	1.08 (0.85 1.31)	1.82 (0.89 2.75)
b	10.9 (-13.7 35.6)	1.30 (-12.95 15.56)
Goodness of fit		
SSE	322.5	144.8
R-square	0.98	0.92
Adjusted R-square	0.98	0.90
RMSE	10.3	6.94

3.6.0.2 Relationships between observations To complete the statistical charac-
terization, we computed the skewness S and kurtosis K, which are indicators of the sym-
metry and the intermittency, respectively, of the observed variable (**Fig. 7.a**). The re-
lationship between kurtosis K and skewness S of the different measured parameters was
assessed by fitting a quadratic function $K = aS^2 + b$ for ϵ and N^2 (fit parameters can
be found in **Tab. 1.c**). Additionally, theoretical curves for the log-normal and Gamma
distributions are presented to allow for a comparison. Our statistics reproduce the same
behaviour as in Lozovatsky et al. [2017]. The quadratic relationship fits well the dissi-
pation rate observations (**Fig. 7.a**, squares over the black line) whose distribution is closer
to the Gamma than to the log-normal distribution. Regarding the absolute values of the
high order statistics, the stratified bins B1 and B2 are less symmetric and intermittent
than for the surface bins W1 and W2, with the bottom bin BBL standing in between
while being closer to the latter. Median values of ϵ (**Fig. 7.b**) indicate a partition be-
tween stratified and mixed layers, decreasing from 11×10^{-10} W kg^{-1} in the transitional
period summer-to-fall ($W1$ in green) to 4×10^{-10} W kg^{-1} in winter ($W2$ in cyan). The
strongest median values are around 13×10^{-10} W kg^{-1} and concern the stratified bins
($B1$ in blue, and $B2$ in red). In term of distribution, N^2 (**Fig. 7.a**) appear to be close
to the log-normal distribution for the stratified bins (B1 in blue triangle, B2 in red, and
BBL in gray), and differ in the mixed layers (W1 in green triangle and W2 in cyan). Its
kurtosis (and skewness, not shown) clearly decreases in function of the intensity of the
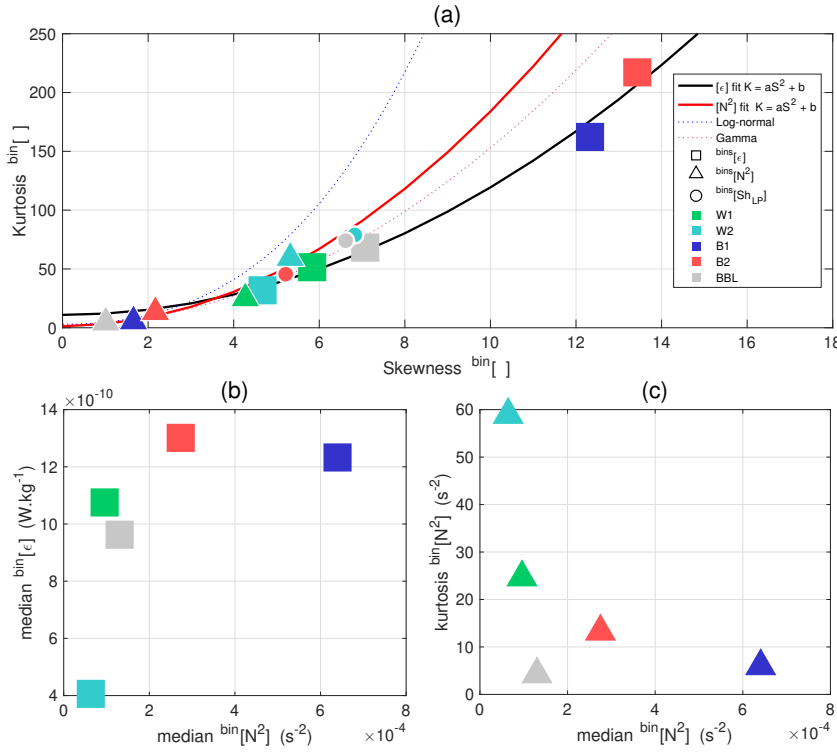stratification (**Fig. 7.c**).

Figure 7: (a) Skewness (S) and kurtosis (K) of ϵ (squares), N^2 (triangles), and Sh_{LP}
(dots), for the different temporal and vertical groups of data (colors refer to the bins on
Fig. 2.c). A discussion dedicated to Sh_{LP} is given in the Appendix. Black and red plain
lines indicate quadratic fits $K = aS^2 + b$ as proposed by Lozovatsky et al. [2017] and
applied to ϵ and N^2. Statistics of the parameters can be consulted in Tab. 1. Blue and
red dashed lines indicates theoretical curves for log-normal and Gamma distributions. (b)
Median of ϵ (W kg^{-1}) and (c) kurtosis of N^2 (s^{-2}), in function of the median of N^2 (s^{-2}).

4 Discussion

We used CTD and microstructure observations to depict the time evolution of the water column in the Gulf of Naples, a mid-latitude non-tidal coastal site. This data set showed a deepening of the ML starting in late summer, marked by intermittent high dissipation rates below the MLD. Closer to the surface, we observed short periods of enhanced turbulence that may contribute to the deepening of the ML. We review here some mechanisms potentially relevant to explain our coastal observations, synthesised schematically on **Fig. 8**.

Figure 8: Schematic representation of the relevant processes identified in this study for seasonal destratification cycle, at the LTER-MC site in the Gulf Of Naples, by 75m deep, from July 2015 to February 2016. Freshwater (blue dashed arrows), wind stress (gray arrows) and buoyancy fluxes (red arrows) are represented at the surface. The salty tongue observed in the hydrology is depicted in dashed dark blue, while the turbid bottom layer is shown in brown. The MLD is schematized in thick gray. The two regions occupied by the first two baroclinic modes of internal waves (IW) are indicated by the shaded layers below the MLD. Schematic patches showing intensified turbulent kinetic energy dissipation rates are plotted in orange. Salt fingering (SF) and diffusive convection regimes are schematized by the blue stairs and the yellow circles, respectively.

The shallow waters of the GoN are strongly influenced by the atmospheric forcings. Positive buoyancy fluxes in summer (**Fig. 8**, pink arrow pointing down) maintain a strong stratification that light summer winds (**Fig. 8**, black curly lines) can hardly break. Storms started at the end of summer with dominating enhanced wind episodes and the first negative buoyancy fluxes (**Fig. 8**, pink arrow pointing up), both contributing to a deepening of the ML. Fall and winter periods were marked by increasingly negative buoyancy fluxes and few intermittent episodes of strong wind.

Regarding the water column T-S properties, the close-by Sarno River, located in the northeast corner of the GoN (**Fig. 1**), is a potential source of freshwater anomalies propagating along the east side of the Gulf. This river could thus be the main source of the low salinity content of surface waters observed from July to October (**Fig. 8**, vertical dashed blue arrows) even if the study of Cianelli et al. [2012] showed that this in-

fluence should be constrained to the eastern part of the GoN. Satellite observations in recent studies of the regional circulations suggest an indirect influence of the Volturno river located in the Gulf of Gaeta (to the northwest and out of the GoN), whose nutrient-rich waters may reach the GoN through mesoscale and submesoscale features forced by the westerly wind events (Iermano et al. [2012]). A local pooling effect could exist in summer, with freshwater trapped at the coast by the daily oscillation of breeze winds (Cianelli et al. [2017]). The nearby Tyrrhenian sea instead acts as a source for the salty waters that were observed at depth from July to October, and over the whole water column later in the year (**Fig. 8**, dashed dark blue line). These salty intrusions into the GoN are possibly at the origin of the salt-fingers patterns we identified and related to the the fine density steps we observed in our data set (**Fig. 8**, blue stairs). These steps-like features are present the coastal area, but manifesting on smaller scales than the typical Tyrrhenian stairs (Durante et al. [2019]). There, they may be related to interleaving events (Ruddick & Richards [2003]), and their vertical structure in layers of 0.3 to 3 m-thick is coherent with the case of a strong stratification and intermittent and weak mixing (Linden [1976], Turner [1983]). Double diffusive processes could be at the origin of a net transfer of mass toward the bottom layers and they could play an important role for the vertical transfer of nutrients available for biological species (Ruddick & Turner [1979]). The impact of salt-fingering on the duration of the stratified period remains to be quantified, even in such coastal areas where they are usually assumed to be insignificant. During the fall season, the unstable vertical salinity gradients progressively weakened, making subsurface layers more prone to diffusive convection (**Fig. 8**, yellow circles).

These upper layer processes that contribute to the ML deepening found their energy source in the atmospheric forcings. Below the ML, the energy for sustaining the mixing is possibly brought by internal wave activity as the sheared layers suggest (**Fig. 8**, gray shaded layers). Measurements of the large scale shear are planned for future cruises to try to quantify this energy transfer.

Next, we consider various mechanisms that may be relevant to explain the seasonal succession of mixing events. Due to the specific vertical structure observed in the GoN during the stratified period, with warm salty waters overlying cooler and fresher waters, salt-fingering can be active. This provides a particular hydrological context for the generation, propagation and mixing of internal waves (Inoue et al. [2007], Maurer & Linden [2014]). Locally, internal waves could also be generated by wind-driven rapid deepening, supported also by Langmuir motions forced by the surface wave field (Polton et al. [2008]). It is noteworthy that we did not sample during storms, which also act as local sources of internal waves. The proximity of the coast could play an important role in forcing internal waves, following the recent study of Kelly [2019]. They found that a coastal reflection of wind-driven inertial oscillations in the ML could generate offshore propagating near-inertial waves, associated to an intensified shear in the region below the ML (e.g. their Fig. 8). Indeed, the GoN coast is only 2 km away from the sampling site and we observed an intensification of shear events during the fall season, characterised by intense storminess and intermediate MLDs. Therefore, this specific mechanism could contribute to create these vertical shear events we observed in correspondence of the main baroclinic modes. In turn, this could contribute to the destratification of the water column during the transition to the winter state. The morphology of the GoN could be a source of internal waves generation too. Internal waves generated by current-topography interaction can radiate from the shelf to the coast with strong imprint on the first two baroclinic modes (Xie & Li [2019]). The existence of steep canyons in the GoN, and notably the Dohrn Canyon at south, provides a topographical configuration that could act as source for the generation of on-shore propagating waves. A current-topography interaction could be sustained also by the various bathymetrical features close to the coast (the Banco della Montagna, the Ammontatura channel and the Mt. Somma-Vesuvius complex on Fig. 1 in Passaro et al. [2016], located south, southwest and northeast from

the LTER-MC sampling point). Finally, a recurrent transition of Kelvin coastal trapped waves over the area has been proposed in the numerical study by de Ruggiero et al. [2018].

The oceanic response to climate change involves several processes, with various degrees of complexity. To reach a full predictive capability it is important to characterise their respective roles and the associated temporal and spatial variability. The analysis of the distribution of ϵ through the different periods represents a step toward a statistical characterization of ϵ, as investigated by the recent studies on the distribution in the interior ocean (Lozovatsky et al. [2017], Buckingham et al. [2019]). We showed that dissipation rates in the ML follows a Burr XII distribution instead of a lognormal. This result requires further study since a lognormal behaviour is considered as ubiquitous for such intermittent features (Pearson & Fox-Kemper [2018]). The respective roles of temporal intermittency and spatial heterogeneity remain to be determined. Finally, it is to note that the use of a small research vessel did not allow for sampling in rough weather and, therefore, the temporal intermittency is here presumably highly underestimated. This points to the need of microstructure observations that are designed to fully cover the spectrum of space and time scales (Pearson & Fox-Kemper [2018]). These specific challenges have to be met in the next future (Benway et al. [2019]) along with long-term observations to constrain the current climate change. Effort could include the deployment of microstructure devices mounted on moorings and wirewalker systems (Pinkel et al. [2011]), or to design and deploy dedicated drifters that regularly sample the water column as it is the case for the Argo floats (Roemmich et al. [2019]). In addition to following well-known probability distributions, we observed a quadratic relation between kurtosis and skewness in the statistics of ϵ, as it has been shown and discussed in the studies of Schopflocher & Sullivan [2005] and Lozovatsky et al. [2017]. This remarkable fit is quite universal since it does not depend upon the specificity of the physics's laws. It fits quite well also the low pass component of the microstructure shears, that was not used for estimating ϵ. In addition, the low pass shear events have a layer-averaged intensity that is linearly increasing with N^2. Statistics on the degree of intermittency, instead, are specific to the environmental conditions, that is, they are different for the ML and the interior.

Our microstructure survey was part of the long term monitoring of the coastal area of the GoN, by the Marechiara project started in 1984 and running until now. It provided an unique view, from July 2015 to February 2016, on the seasonal cycle of the stratification and mixing in the GoN. In the companion study in preparation, that investigated CTD and forcing data over 2001-2020, we derived the mean seasonal cycles of the water column structure. When compared to the bi-decadal mean cycles it is found that the water column in 2015 was fresher and accumulated relatively less heat, the late summer period being marked by significant rain event and moderate winds. In this study we observed that the long term thermal components (water column heat content, surface temperature) at the sampling site of the GoN did not exhibit increasing decadal trends as those observed over the Mediterranean basin (Pisano et al. [2020]), in contrary of the freshwater components reflecting the redistribution of precipitation at larger scale. So, in addition to a regional warming (e.g., heatwaves), the question of both the influence of larger scale actors (atmospheric systems changes) and intermittent events is to be considered (Baldi et al. [2006])). This promotes the efforts of long-term observations over these coastal areas to better understand the various processes and distinguish among them which ones (if not all) are more sensitive to future climate change. The complexity of mechanisms at finescales whose interplay produce convection, shear, mixing, leading to the ML deepening, can be significantly modulated by long-term heat, freshwater and wind changes (Somavilla et al. [2017]). In conclusion, we suggest that sites such as the GoN, a shelf region in a non-tidal area, are of interest for discriminating between processes less energetic than tides, as internal waves or even double-diffusion, beyond the global warming and the consequent increase of the stratification (Woodson [2018], Guancheng et al. [2020]).

Appendix A Low frequency signals in the microstructure shears data

This section is motivated by the repeated observation of a low-frequency signal in our microstructure shear data, while the instrument's fall speed remained constant. This signal was observed within stratified layers, at the MLD and below the MLD, depicting vertical patterns during our survey (**Fig. A1**). We propose here a first attempt to separate parts of the signal that may be due to strong thermal gradients (pyro-effect, as discussed after), and other ones possibly due to other noise sources, or real energetic motions. The shear probes are sensitive to velocity fluctuations at frequencies greater than 0.1 Hz, but the signals are often high-pass filtered at higher frequencies ($\sim$0.4 Hz) before computing the spectra and the dissipation rate. Here we intended to carefully use the low frequency part of shear signals since no other sources of velocity shear were available. However, it is most likely that the low-frequency response in the micro-structure shear data is due to passing through strong thermal gradients, an effect known as the pyro-electric effect, which cannot be interpreted as a physical shear signal (see below). Despite this, an analysis of the low frequency signal still shows some interesting patterns that are worth presenting.

For the analysis, we defined low-passed shear energy estimates $Sh_{LP}^{1,2}$ from shear 1 and 2, calculated by low-pass filtering the despiked shears at 0.1 Hz, as
$$Sh_{LP}^{1,2} = \langle\, (du/dz)^2\, \rangle_{LP}^{0.1Hz}, \quad \langle\, (dv/dz)^2\, \rangle_{LP}^{0.1Hz}.$$
In our dataset, structures linked to this low-frequency signal showed vertical scales of around 3 m. We show on **Fig. A1** time filtered quantities at 0.1 Hz, that are equivalent to a spatial filtering over these length scales. We note that spatial filtering has the advantage to avoid numerical negative values (e.g. if used to estimate a proper energy content).
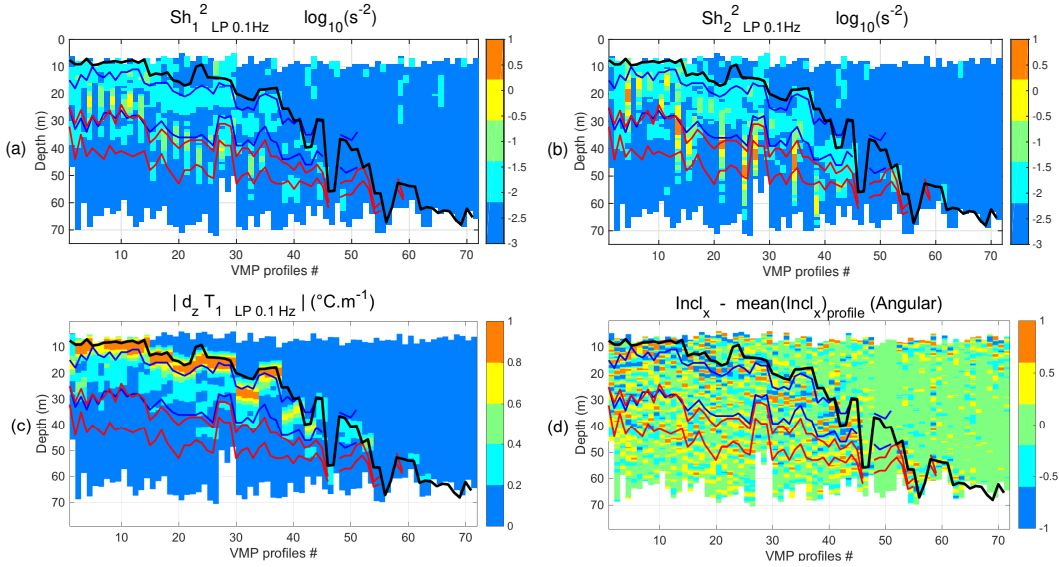

Figure A1: Square value of the microstructure shears 1 (a) and 2 (b) (i.e. du/dz and dv/dz, respectively) low pass filtered at 0.1 Hz (s^{-2}). We plotted the absolute values due to numerical negative values created by the filtering after the square operator. Profiles examples are shown on supplementary Fig. S3. (c) Microstructure gradients dT/dz ($^\circ$ m^{-1}) low-passed filtered at 0.1 Hz, and plotted in absolute value, showing subsurface layers concerned by strong vertical thermal gradients. These are mainly located between the base of the MLD and the upper limit of the envelope of the baroclinic mode B1. (d) Anomaly to the mean value of the roll inclination of the `VMP-250` (angular $^\circ$ relative to the x-axis).

Pyro-electric effect

Shear probes occasionally respond to large changes in temperature with the sudden release (or absorption) of electric charge that generates a large amplitude signal, even when no strain is applied to the ceramic beam (Lueck et al. [2002]). This effect is referred to as the pyro-electric effect (Muralt [2005]) and can occur when probes pass through large temperature gradients. To minimize this effect, the piezo-ceramic element in the shear probe is insulated from the environment by a layer of epoxy and the electronics are designed to high-pass filter the signal at 0.1 Hz (Rockland's Technical Note 005). Despite these precautions in the sensor design, some shear probes may still respond to sharp changes in temperature. In this study, the response was somewhat unpredictable and probe-dependent.

This signal was present in the subsurface shear data, when the profiler passed through the strong seasonal vertical gradients of temperature, leading to contamination of the shear signal at low frequencies between 0.1 and 1 Hz. The amplitude of the temperature gradient at the base of the MLD was approximately $1\,^\circ\,\mathrm{m}^{-1}$ in summer, to $0.3\,^\circ\,\mathrm{m}^{-1}$ during the transition from fall to winter (**Fig. A1.c**). The two shear probes responded differently when crossing the same vertical temperature gradient: shear 1 appeared to be less sensitive than shear 2 in general, with values of 3 times smaller in average, and less concerned by surface gradients. In general the resulting low-frequency signal was present up to nearly 1 Hz. To avoid temperature contamination of dissipation rate estimates in the rest of our study, we applied a high-pass filtering with a cut-off frequency of 1.5 Hz on the despiked micro-structure shears before using them to compute the spectra and estimate ϵ (see Methods). We considered the spare probe shear 2 suitable for estimating ϵ from its high-frequency content, but its low-frequency signal is probably contaminated by pyro-effect on subsurface, and intensified noisy response in the deep layers.

Low-frequency content below the strong surface gradients

As visible on (**Fig. A1**), a repetitive low frequency signal was intermittently present too in the deep layers at a 20m-distance below the MLD, both on shear 1 and 2. In contrary of the surface, these layers are concerned by moderated thermal gradients, and the shear response to this vertical structure should be presumably be free from pyro-electric contamination. We observe that this signal is distributed through the vertical envelope of the baroclinic modes of internal waves (as we defined it), and is frequently associated with small and slow oscillations of $\pm\, 2°$ of the instrument roll (**Fig. A1.d**), even no specific noise contamination was visible through the accelerometers. Moreover, it appears to be co-located with other independent physical parameters, as we show it on the physical examples taken from the distinct CTD cast and the fluorometer sensor on supplementary Fig. S3. Out of affirming that we identified here a physical signal in the micro-structure shear, we decided to carry apart this low frequency shear signal through our analysis, to show its statistics, as we separated it properly from the high-passed shear used to infer ϵ. We selected only the estimation based on shear 1. To avoid numerical negative values and estimate a proper energy content, we filtered spatially instead of temporally and propose $Sh_{LP} = \langle\, (du/dz)^2\, \rangle_{LP}^{3m}$.

Possible link between Sh_{LP} and ϵ

The stratified layers possibly containing internal wave activity were remarkably co-located with the low-passed energy component Sh_{LP} events, the latter potentially being a proxy of energetic motions, even though its values are challenging to interpret. In particular, two regions exhibit enhanced low pass shear levels (**Fig. A2.a**). The first one is associated with the baroclinic mode region B1: a clear intensification is located below the MLD and follows its deepening from July to early October while another maximum is located around 20-30 m in July and early August. The second one is associated
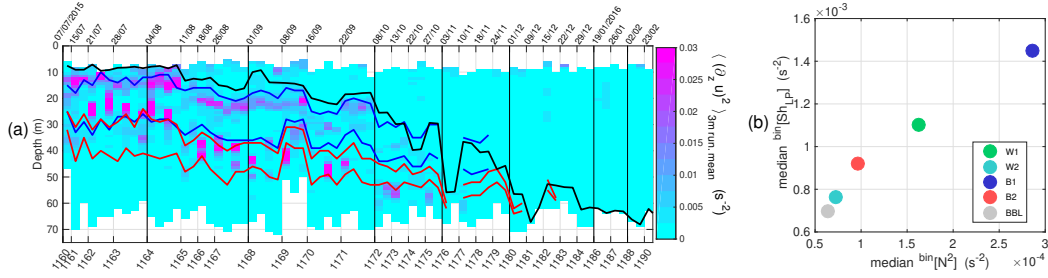
Figure A2: (a) Low pass shear energy Sh_{LP} i.e. $\langle (\partial_z u)^2 \rangle_{LP}^{3m}$ (s^{-2}), $MLD_{\theta_0}^{0.4^\circ C}$ (thick black line), region of maximum energy of baroclinic mode 1 (between blue lines) and mode 2 (between red lines). The VMP profiles are plotted sequentially along the x-axis, where the MC casts references are indicated (from one to four VMP profiles by cast). Sampling dates are given on the panel top. (b) Median of Sh_{LP} (s^{-2}) in function of the median of N^2 (s^{-2}).

with B2 and it is clearly visible during August and September while having less intense imprint in July and October. Elsewhere, the low pass shear is weak whenever the stratification is weak (e.g., ML and BBL). Pdfs are shown in the supplementary information (Fig. S4). Although Sh_{LP} and ϵ are estimated over totally independent wavenumber ranges, their kurtosis-skewness relationship follows the same quadratic fit out of the log-normality (**Fig. 7.a**, dots and squares). In addition, Sh_{LP} shows a remarkable linearity as a function of the stratification intensity (**Fig. A2.b**), while ϵ does not show such a linear relationship with the stratification (**Fig. 7.a**). The Sh_{LP} estimate presented here is not conventional and its interpretation would require a thoughtful validation via a comparison with Acoustic Doppler Current Profiler (ADCP) observations. While to be considered with great caution, we documented in Fig. S5 the distribution of ϵ in function of N^2 and Sh_{LP} as proxy of the shear (Gill [1982], Monin & Yaglom [2007]). Interestingly, it shows higher ϵ values in correspondence with a weaker stratification and larger shear values. The dependence from the stratification intensity is lost in the ML (W1 and W2), while a modulation by N is suggested in the stratified layers B1, B2 and BBL, following the observations of Vladoiu et al. [2018] that tested a wave-wave parameterization for ϵ based on MacKinnon & Gregg [2003] .

References

Albanese, S., Iavazzo, P., Adamo, P., Lima, A., & De Vivo, B. (2012, 09). Assessment of the environmental conditions of the sarno river basin (south italy): A stream sediment approach. *Environmental Geochemistry and Health*, *35*. doi: 10.1007/s10653-012-9483-x

Baldi, M., Dalu, G., Maracchi, G., Pasqui, M., & Cesarone, F. (2006, 09). Heat

waves in the mediterranean: A local feature or a larger-scale effect? *International Journal of Climatology*, *26*, 1477–1487. doi: 10.1002/joc.1389

Barton, A., Ward, B., Williams, R., & Follows, M. (2014, 04). The impact of fine-scale turbulence on phytoplankton community structure. *Limnology and Oceanography: Fluids and Environments*, *4*. doi: 10.1215/21573689-2651533

Benway, H. M., Lorenzoni, L., White, A. E., Fiedler, B., Levine, N. M., Nicholson, D. P., ... Letelier, R. M. (2019). Ocean time series observations of changing marine ecosystems: An era of integration, synthesis, and societal applications. *Frontiers in Marine Science*, *6*, 393. doi: 10.3389/fmars.2019.00393

Brainerd, K. E., & Gregg, M. C. (1995). Surface mixed and mixing layer depths. *Deep-Sea Research I*, *42*, 1521–1543.

Brody, S. R., , & Lozier, M. S. (2014). Changes in dominant mixing length scales as a driver of subpolar phytoplankton bloom initiation in the north atlantic. *Geophysical Research Letter*, *41 (9)*, 3197–3203.

Buckingham, C. E., Lucas, N. S., Belcher, S. E., Rippeth, T. P., Grant, A. L. M., , & Lesommer, J. (2019). The contribution of surface and submesoscale processes to turbulence in the open ocean surfaceboundary layer. *Journal of Advances in Modeling Earth Systems*, *11*, 4066–4099. doi: https://doi.org/10.1029/2019MS001801

(C3S), C. C. C. S. (2017). Era5: Fifth generation of ecmwf atmospheric reanalyses of the global climate. *Copernicus Climate Change Service Climate Data Store (CDS), date of access*. doi: https://cds.climate.copernicus.eu/cdsapp#!/home

Cianelli, D., D'Alelio, D., Uttieri, M., Sarno, D., Zingone, A., Zambianchi, E., & Ribera d'Alcala, M. (2017, 12). Disentangling physical and biological drivers of phytoplankton dynamics in a coastal system. *Scientific Reports*, *7*. doi: 10.1038/s41598-017-15880-x

Cianelli, D., Uttieri, M., Buonocore, B., Falco, P., Zambardino, G., & Zambianchi, E. (2012, 08). Dynamics of a very special mediterranean coastal area: the gulf of naples. *Mediterranean Ecosystems: Dynamics, Management and Conservation*, 129–150.

de Boyer Montégut, C., Madec, G., Fischer, A. S., Lazar, A., & Iudicone, D. (2004, 01). Mixed layer depth over the global ocean: An examination of profile data and profile-based climatology. *Journal of Geophysical Research*, *109*, C12003. doi: 10.1029/2004JC002378

de Ruggiero, P., Ernesto, N., Iacono, R., Pierini, S., & Spezie, G. (2018, 09). A baroclinic coastal trapped wave event in the gulf of naples (tyrrhenian sea). *Ocean Dynamics*. doi: 10.1007/s10236-018-1221-1

Durante, S., Schroeder, K., Mazzei, L., Pierini, S., Borghini, M., & Sparnocchia, S. (2019, 01). Permanent thermohaline staircases in the tyrrhenian sea. *Geophysical Research Letters*. doi: 10.1029/2018GL081747

Ferrari, R., & Wunsch, C. (2009). Ocean circulation kinetic energy: Reservoirs, sources, and sinks. *Annual Review of Fluid Mechanics*, *41*, 253–282.

Garrett, C., Keeley, J., & Greenberg, D. (1978, 12). Tidal mixing versus thermal stratification in the bay of fundy and gulf of maine. *Atmosphere-Ocean*, *16*, 403–423. doi: 10.1080/07055900.1978.9649046

GEBCO, C. G. (2020). *Gebco 2020 grid.* Retrieved from https://www.gebco.net doi: 10.5285/a29c5465-b138-234d-e053-6c86abc040b9

Gill, A. (1982, 01). Atmosphere-ocean dynamics. In (Vol. 30, p. 662).

Goodman, L., Levine, E. R., , & Lueck, R. G. (2006). On measuring the terms of the turbulent kinetic energy budget from an auv. *Journal of Atmospheric and Oceanic Technology*, *23*, 977–990.

Guancheng, l., Cheng, L., Zhu, J., Trenberth, K., Mann, M., & Abraham, J. (2020, 09). Increasing ocean stratification over the past half-century. *Nature Climate Change*, 1–8. doi: 10.1038/s41558-020-00918-2

Hegerl, G. C., Black, E., Allan, R. P., Ingram, W. J., Polson, D., Trenberth, K. E.,

749   . . . Zhang, X. (2015). Challenges in quantifying changes in the global water cycle.
750   *Bulletin of the American Meteorological Society*, *96(7)*, 1097–1115.

751 Iermano, I., Liguori, G., Iudicone, D., Buongiorno Nardelli, B., Colella, S., Zingone,
752   A., . . . Ribera d'Alcala, M. (2012). Dynamics of short-living filaments and their
753   relationship with intense rainfall events and river flows. *Progress in Oceanography*,
754   *106*, 118–137. doi: 10.1016/j.pocean.2012.08.003

755 Inoue, R., Yamazaki, H., Wolk, F., Kono, T., & Yoshida, J. (2007, 03). An estima-
756   tion of buoyancy flux for a mixture of turbulence and double diffusion. *Journal of*
757   *Physical Oceanography*, *37*. doi: 10.1175/JPO2996.1

758 Johnston, T., & Rudnick, D. (2009, 03). Observations of the transition layer. *Jour-*
759   *nal of Physical Oceanography*, *39*. doi: 10.1175/2008JPO3824.1

760 Kelly, S. (2019, 09). Coastally generated near-inertial waves. *Journal of Physical*
761   *Oceanography*, *49*. doi: 10.1175/JPO-D-18-0148.1

762 Kiørboe, T., & Mackenzie, B. (1995, 12). Turbulence-enhanced prey encounter rates
763   in larval fish: Effects of spatial scale, larval behaviour and size. *Journal of Plank-*
764   *ton Research*, *17*, 2319–2331. doi: 10.1093/plankt/17.12.2319

765 Koseki, S., Mooney, P., Cabos Narvaez, W. D., Gaertner, m., de la Vara, A., & Ale-
766   man, J. (2020, 07). Modelling a tropical-like cyclone in the mediterranean sea
767   under present and warmer climate.
768   doi: 10.5194/nhess-2020-187

769 Large, W., & Pond, S. (1981, 01). Open ocean momentum flux measurement in
770   moderate to strong winds. *Journal of Physical Oceanography*, *11*, 336–342.

771 Linden, P. (1976, 10). The formation and destruction of fine-structure by double-
772   diffusive processes. *Deep Sea Research and Oceanographic Abstracts*, *23*, 895–908.
773   doi: 10.1016/0011-7471(76)90820-2

774 Lozovatsky, I., H.J.S., F., J., P.-M., Liu, Z., Lee, J. H., & Jinadasa, S. (2017, 08).
775   Probability distribution of turbulent kinetic energy dissipation rate in ocean:
776   Observations and approximations. *Journal of Geophysical Research*, *122*. doi:
777   10.1002/2017jc013076

778 Lueck, R. (2016). Rsi technical note 028 : Calculating the rate of dissipation of tur-
779   bulent kinetic energy. *Rockland Scientific International Inc.*.

780 Lueck, R., Wolk, F., & Yamazaki, H. (2002, 02). Oceanic velocity microstructure
781   measurements in the 20th century. *Journal of Physical Oceanography*, *58*, 153–
782   174. doi: 10.1023/A:1015837020019

783 MacKinnon, J., & Gregg, M. (2003, 07). Mixing on the late-summer new england
784   shelf—solibores, shear, and stratification. *Journal of Physical Oceanography*, *33*,
785   1476–1492. doi: 10.1175/1520-0485(2003)033⟨1476:MOTLNE⟩2.0.CO;2

786 Mackinnon, J. A., & Gregg, M. C. (2005). Near-inertial waves on the new england
787   shelf: The role of evolving stratification, turbulent dissipation, and bottom drag.
788   *Journal of Physical Oceanography*, *35*, 2408–2424.

789 Mann, K. H., & Lazier, J. R. N. (1996). *Dynamics of marine ecosystems*.

790 Maurer, B., & Linden, P. (2014, 08). Intrusion-generated waves in a linearly strati-
791   fied fluid. *Journal of Fluid Mechanics*, *752*, 282–295. doi: 10.1017/jfm.2014.316

792 McDougall, T., & Barker, P. (2011). Getting started with teos-10 and the gibbs sea-
793   water (gsw) oceanographic toolbox. *SCOR/IAPSO WG*, *127*, 1—28.

794 Monin, A., & Yaglom, A. (2007). *Statistical fluid mechanics, volume 1: Mechanics of*
795   *turbulence*.

796 Muralt, P. (2005). Pyroelectricity. In F. Bassani, G. L. Liedl, & P. Wyder (Eds.),
797   *Encyclopedia of condensed matter physics* (pp. 441–448). Oxford: Elsevier. doi: 10
798   .1016/B0-12-369401-9/00434-4

799 Nuttall, A. H. (1971). Spectral estimation by means of overlapped fast fourier trans-
800   form processing of windowed data. *NUSC Tech. Rep. No. 4169*. doi: https://apps
801   .dtic.mil/sti/pdfs/AD0739315.pdf

Obukhov, A. (n.d.). Turbulentnost'v temperaturnojneodnorodnoj atmosfere ("turbulence in an atmosphere with a non-uniform temperature"). *Tr. Inst. Teor. Geofiz. Akad. Nauk. SSSR.*, *1*, 95—115.

Obukhov, A. (1971, 01). Turbulence in an atmosphere with non-uniform temperature. *Boundary-Layer Meteorology*, *2*, 7–29. doi: 10.1007/BF00718085

Osborn, T. (1998, 01). Finestructure, microstructure, and thin layers. *Oceanography*, *11*. doi: 10.5670/oceanog.1998.13

Passaro, S., Tamburrino, S., Vallefuoco, M., Gherardi, S., Sacchi, M., & Guido, V. (2016, 06). High-resolution morpho-bathymetry of the gulf of naples, eastern tyrrhenian sea. *Journal of Maps*, 1–8. doi: 10.1080/17445647.2016.1191385

Pastor, F., Valiente, J. A., , & Palau, J. L. (2018). Sea surface temperature in the mediterranean: Trends and spatial patterns (1982–2016). *Pure and Applied Geophysics*, *175*, 4017—4029. doi: https://doi.org/10.1007/s00024-017-1739-z

Pearson, B., & Fox-Kemper, B. (2018, 02). Log-normal turbulence dissipation in global ocean models. *Physical Review Letters*, *120*. doi: 10.1103/PhysRevLett.120.094501

Pingree, R., Holligan, P., Mardell, G., & Head, R. (1976, 11). The influence of physical stability on spring, summer and autumn phytoplankton blooms in the celtic sea. *Journal of the Marine Biological Association of the United Kingdom*, *56*, 845–873. doi: 10.1017/S0025315400020919

Pinkel, R., Goldin, M., Smith, J., Sun, O., Aja, A., Bui, M., & Hughen, T. (2011, 03). The wirewalker: A vertically profiling instrument carrier powered by ocean waves. *Journal of Atmospheric and Oceanic Technology*, *28*, 426–435. doi: 10.1175/2010JTECHO805.1

Pisano, A., Marullo, S., Artale, V., Falcini, F., Yang, C., Leonelli, F., . . . Buongiorno Nardelli, B. (2020, 01). New evidence of mediterranean climate change and variability from sea surface temperature observations. *Remote Sensing*, *12*. doi: 10.3390/rs12010132

Polton, J., Smith, J., Mackinnon, J., & Tejada-Martínez, A. (2008, 07). Rapid generation of high-frequency internal waves beneath a wind and wave forced oceanic surface mixed layer. *Geophysical Research Letters*, *35*. doi: 10.1029/2008GL033856

Prairie, J., Sutherland, K., Nickols, K., & Kaltenberg, A. (2012, 04). Biophysical interactions in the plankton: A cross-scale review. *Limnology and Oceanography: Fluids and Environments*, *2*. doi: 10.1215/21573689-1964713

Ribera d'Alcala, M., Conversano, F., Corato, F., Licandro, P., Mangoni, O., Marino, D., . . . Zingone, A. (2004, 04). Seasonal patterns in plankton communities in pluriannual time series at a coastal mediterranean site (gulf of naples): An attempt to discern recurrences and trends. *Scientia Marina*, *68*, 65–83.

Roemmich, D., Alford, M., Claustre, H., Johnson, K., King, B., Moum, J., . . . Yasuda, I. (2019, 08). On the future of argo: A global, full-depth, multi-disciplinary array. *Frontiers in Marine Science*, *6*. doi: 10.3389/fmars.2019.00439

Ruddick, B. (1983, 10). A practical indicator of the stability of the water column to double-diffusive activity. *Deep Sea Research Part A. Oceanographic Research Papers*, *30*, 1105–1107. doi: 10.1016/0198-0149(83)90063-8

Ruddick, B., Anis, A., & Thompson, K. (2000, 11). Maximum likelihood spectral fitting: The batchelor spectrum. *Journal of Atmospheric and Oceanic Technology*, *17*, 1541–1555. doi: 10.1175/1520-0426(2000)017⟨1541:MLSFTB⟩2.0.CO;2

Ruddick, B., & Richards, K. (2003, 03). Oceanic thermohaline intrusions: Observations. *Progress In Oceanography*, *56*, 499–527. doi: 10.1016/S0079-6611(03)00028-4

Ruddick, B., & Turner, J. (1979, 08). The vertical length scale of double-diffusive intrusions. *Deep Sea Research Part A. Oceanographic Research Papers*, *26*, 903–913. doi: 10.1016/0198-0149(79)90104-3

Schopflocher, T., & Sullivan, P. (2005, 06). The relationship between skewness and kurtosis of a diffusing scalar. *Boundary-Layer Meteorology*, *115*, 341–358. doi: 10 .1007/s10546-004-5642-7

Shang, X., Qi, Y., Chen, G., Liang, C., Lueck, R., Prairie, B., & Li, H. (2016, 10). An expendable microstructure profiler for deep ocean measurements. *Journal of Atmospheric and Oceanic Technology*, *34*. doi: 10.1175/JTECH-D-16-0083.1

Skliris, N., Marsh, R., Josey, S. A., Good, S. A., Liu, C., & Allan, R. P. (2014). Salinity changes in the world ocean since 1950 in relation to changing surface freshwater fluxes. *Climate Dynamics*, *43*(3-4), 709–736. doi: 10.1007/ s00382-014-2131-7

Somavilla, R., Gonzalez-Pola, C., , & Fernandez-Diaz, J. (2017). The warmer the ocean surface, the shallower the mixed layer. how much of this is true? *Journal of Geophysical Research*, *122*(9), 7698–7716. doi: 10.1002/2017JC013125

Sverdrup, H. (1953, 01). On conditions for the vernal blooming of phytoplankton. *J. Cons. int. Explor. Mer*, *18*, 287–295. doi: 10.1093/icesjms/18.3.287

Thorpe, S. A. (2005). *The turbulent ocean.* Cambridge University Press.

Turner, J. (1967, 10). Salt fingers across a density interface. *Deep Sea Research and Oceanographic Abstracts*, *14*, 599-611. doi: 10.1016/0011-7471(67)90066-6

Turner, J. (1973, 01). Buoyancy effects in fluids. doi: 10.1017/CBO9780511608827

Turner, J. (1983). Oceanic fine and microstructure. *Brewer P.G. (eds) Oceanography*.

Vladoiu, A., Bouruet-Aubertot, P., Cuypers, Y., Ferron, B., Schroeder, K., Borghini, M., ... Ben Ismail, S. (2018, 05). Turbulence in the sicily channel from microstructure measurements. *Deep Sea Research Part I: Oceanographic Research Papers*. doi: 10.1016/j.dsr.2018.05.006

Volosciuk, C., Maraun, D., Semenov, V. A., Tilinina, N., Gulev, S. K., , & Latif, M. (2016). Rising mediterranean sea surface temperatures amplify extreme summer precipitation in central europe. *Scientific Reports*, *6*(32450). doi: 10.1038/srep32450

Wheeler, J. D., Secchi, E., Rusconi, R., , & Stocker, R. (2019). Not just going with the flow: The effects of fluid flow on bacteria and plankton. *The Annual Review of Cell and Developmental Biology*.

Wihsgotta, J. U., Sharples, J., Hopkins, J. E., Woodward, E. M. S., Hulld, T., Greenwood, N., ... Sivyer, D. B. (2019). Observations of vertical mixing in autumn and its e ect on the autumn phytoplankton bloom. *Progress in Oceanography*, *177*.

Wolk, F., Yamazaki, H., Seuront, L., & Lueck, R. (2002, 05). A new free-fall profiler for measuring biophysical microstructure. *Journal of Atmospheric and Oceanic Technology*, *19*. doi: 10.1175/1520-0426(2002)019⟨0780:ANFFPF⟩2.0.CO;2

Woodson, C. (2018, 01). The fate and impact of internal waves in nearshore ecosystems. *Annual Review of Marine Science*, *10*. doi: 10.1146/annurev-marine-121916 -063619

Wunsch, C., & Ferrari, R. (2004). Vertical mixing, energy, and the general circulation of the oceans. *Annual Review of Fluid Mechanics*, *36*, 281–314.

Xie, X., & Li, M. (2019, 04). Generation of internal lee waves by lateral circulation in a coastal plain estuary. *Journal of Physical Oceanography*, *49*. doi: 10.1175/ JPO-D-18-0142.1

Zhang, H.-M., & Talley, L. (1998, 10). Heat and buoyancy budgets and mixing rates in the upper thermocline of the indian and global oceans. *Journal of Physical Oceanography*, *28*, 1961–1978. doi: 10.1175/1520-0485(1998)028⟨1961: HABBAM⟩2.0.CO;2

Zhang, W., Villarini, G., Scoccimarro, E., & Napolitano, F. (2020, 05). Examining the precipitation associated with medicanes in the high-resolution era-5 reanalysis

910   data. *International Journal of Climatology*. doi: 10.1002/joc.6669

911   Zika, J. D., Skliris, N., Nurser, A. J. G., Josey, S. A., Mudryk, L., Laliberte, F.,

912   & Marsh, R.   (2015).   Maintenance and broadening of the ocean's salinity dis-

913   tribution by the water cycle.   *Journal of Climate*, *28*(24), 9550–9560.   doi:

914   10.1175/JCLI-D-15-0273.1

915   Zingone, A., D'Alelio, D., Mazzocchi, M. G., Montresor, M., & Sarno, D.   (2019,

916   05).   Time series and beyond: Multifaceted plankton research at a marine

917   mediterranean lter site.   *Nature Conservation*, *34*, 273–310.   doi: 10.3897/

918   natureconservation.34.30789

Supporting Information for "Microstructure observations of the summer-to-winter destratification at a coastal site in the Gulf of Naples"

Florian Kokoszka[1], Fabio Conversano[1], Daniele Iudicone[1], Bruno Ferron[2],

Pascale Bouruet-Aubertot[3], Justine Mc Millan[4]

[1]Stazione Zoologica Anton Dohrn, Naples, Italy

[2]Univ. Brest, CNRS, IFREMER, IRD, Laboratoire d'Océanographie Physique et Spatiale (LOPS), IUEM, Plouzané, France

[3]Sorbonne Université (UPMC, Univ Paris 06)-CNRS-IRD-MNHN, LOCEAN, Paris, France

[4]Rockland Scientific International Inc., Victoria, Canada

Contents of this file

Introduction We provide in Tab. S1 the list and dates of the CTD casts (referenced as MC), including the sequence of VMP profiles. Statistics of the Turners's regimes by layers

―――――

Corresponding author: F. Kokoszka, Department of Research Infrastructures for Marine Biological Resources (RIMAR), Stazione Zoologica A. Dohrn, villa Comunale, 80121, Naples, Italy (florian.kokoszka@szn.it)

December 1, 2020, 5:45pm

are given in Tab. S2. We provide in Fig. S1 some details of the VMP data processing. The stratification's decomposition through baroclinic modes of internal waves is presented in Fig. S2. Vertical profiles of some MC casts for CTD and VMP data are detailed in Fig. S3. Additional statistics of the Sh_{LP} are presented in Fig. S4 and Fig. S5.

Tab S1. Metadata We present in Tab. S1 the dates and references of CTD and VMP profiles.

Tab S2. Turner's regimes We present in Tab. S2 some statistics from the Turner's analysis.

Fig S1. VMP processing We calculated dissipation rates of turbulent kinetic energy with the ODAS Toolbox provided by Rockland (version 4.4.06). We present on Fig. S1 the quality metric of our data with the Figure of Merit (FM) and two examples of Nasmyth's fit illustrating stratified and weakly stratified water-column cases.

Fig S2. Stratification and baroclinic modes of internal waves Ocean dynamic vertical modes were calculated for each profile from N^2, using the routine from Klink (1999). Profiles were smoothed by filtering over a 10m-length running window before applying the algorithm. We focused then on the two first modes B1 and B2 that presented the largest variances. We defined then some vertical envelopes for the layers of these two modes. For each profile, we considered the layer containing the shear maxima of the first two baroclinic modes. To achieve this, we normalized the shear maxima to 1 and identified the depths interval, as the upper and lower depths of the layer where values were > 0.9. To consider only stratified part of the water-column, calculations were made below the MLD. A comparison between N^2 calculated from both VMP-microCT and CTD hydrology, with a plot of the baroclinic modes and their envelope is shown on Fig. S2.

Fig S3. VMP casts's examples We present on Fig. S3 vertical profiles from the VMP casts MC1173, MC1175 and MC1180 to show some examples of the rich structure of the water-column. Cast MC1180 illustrates a winter case when the MLD reaches the proximity of the bottom layer, where a turbid feature is present from 62 to 70m. In the stratified cases of casts MC1173 and MC1175, even more thin, turbid bottom layers are present too below 60m. Weak double salt fingering layers can be seen too, below the MLD between 25 and 45m, with Tu angles around 60° and 50°, respectively. All casts show intensified Sh_{LP} located below the passage of the local density gradients.

Fig S4. Probability density functions of the low-frequency content of the micro-structure shear The stratified layers possibly containing internal wave activity were remarkably co-located with the low-passed energy component Sh_{LP} (see Appendix) that could be an interesting proxy of energetic motions, even its values are not possible to interpret. A clear pattern is visible (see Fig. A1), with intense occurrences distributed into the highly stratified layers during the summer period, and then into the subsurface layers marking the baroclinic modes $B1$ and $B2$. Two tendencies are visible. A first one below the MLD and B1 in July and early August, and a second one through both B1 and B2 layers from mid-August to the end of October. In terms of distribution (Fig. S4), the most intense values of around 1×10^{-3} s^{-2} are contained into the bins below the MLD in the B1 bin (Fig. S4.b). Surface layers are dominated by weaker values of around 6×10^{-2} s^{-2} (Fig. S4.a).

Fig S5. Dissipation rates in function of N^2 and Sh_{LP} Even Sh_{LP} is challenging to use and interpret, a classical display averaged values of ϵ ($W.kg^{-1}$) by intervals ΔN^2 (s^{-2}) and ΔSh_{LP} (s^{-2}) is shown on Fig. S5.

Table S1.   General information of the MC-CTD casts and VMP profiles.

VMP#	CTD# (MC cast)	Date	VMP#	CTD# (MC cast)	Date	VMP#	CTD# (MC cast)	Date
1	1160	07/07/2015 08:01	24	1168	01/09/2015 07:46	47	1176	03/11/2015 09:31
2	1161	15/07/2015 09:39	25	1168	01/09/2015 08:40	48	1177	10/11/2015 09:24
3	1161	15/07/2015 09:41	26	1168	01/09/2015 08:43	49	1177	10/11/2015 09:27
4	1162	21/07/2015 08:04	27	1169	08/09/2015 07:57	50	1178	18/11/2015 09:23
5	1162	21/07/2015 08:07	28	1169	08/09/2015 08:00	51	1178	18/11/2015 09:25
6	1162	21/07/2015 08:55	29	1169	10/09/2015 08:46	52	1179	24/11/2015 09:49
7	1163	28/07/2015 08:23	30	1170	16/09/2015 08:27	53	1179	24/11/2015 09:52
8	1163	28/07/2015 09:26	31	1170	16/09/2015 08:30	54	1180	01/12/2015 09:08
9	1163	28/07/2015 09:29	32	1170	16/09/2015 10:18	55	1180	01/12/2015 09:11
10	1163	28/07/2015 08:20	33	1170	16/09/2015 10:21	56	1181	09/12/2015 09:27
11	1164	04/08/2015 07:49	34	1171	22/09/2015 07:55	57	1181	09/12/2015 09:30
12	1164	04/08/2015 07:51	35	1171	22/09/2015 07:58	58	1182	15/12/2015 09:32
13	1164	04/08/2015 08:45	36	1171	22/09/2015 08:53	59	1182	15/12/2015 09:35
14	1164	04/08/2015 08:48	37	1171	22/09/2015 08:56	60	1183	22/12/2015 09:01
15	1165	11/08/2015 08:11	38	1172	08/10/2015 08:38	61	1183	22/12/2015 09:04
16	1165	11/08/2015 08:14	39	1172	08/10/2015 08:40	62	1184	29/12/2015 09:01
17	1166	18/08/2015 07:55	40	1173	13/10/2015 08:21	63	1184	29/12/2015 09:04
18	1166	18/08/2015 07:58	41	1173	13/10/2015 08:24	64	1186	19/01/2016 08:36
19	1167	26/08/2015 07:34	42	1174	22/10/2015 08:09	65	1186	19/01/2016 08:39
20	1167	26/08/2015 07:37	43	1174	22/10/2015 08:12	66	1187	26/01/2016 09:59
21	1167	26/08/2015 08:59	44	1175	27/10/2015 09:34	67	1187	26/01/2016 10:02
22	1167	26/08/2015 09:02	45	1175	27/10/2015 09:37	68	1188	02/02/2016 11:29
23	1168	01/09/2015 07:44	46	1176	03/11/2015 09:28	69	1188	02/02/2016 11:32
						70	1190	23/02/2016 10:19
						71	1190	23/02/2016 10:22

December 1, 2020, 5:45pm

Table S2. (a) Decibar occupation of the Turner's regimes for the whole dataset. (b) Statistics

by layers and period bins for the double diffusive and (c) diffusive convection regimes.

(a) General

Regime	SF	Stable	Diffusive	Instable	All
Count	1202	2159	396	142	3899
%	30.8%	55.4%	10.2%	3.6%	100

(b) Double diffusive regime (salt fingers)

Bin	%	mean Tu mean R_ρ	median	std	SF%	Stable%	Diff.%	Inst.%	Bin count
All	100	54.7 (Tu) 8.88 (R_ρ)	51.8 6.79	9.3 6.82	30.80	55.4	10.2	3.6	3899
surface-MLD	32	60.5 6.03	58.7 3.77	11.2 5.67	24.7	41.8	25	8.5	1573
MLD-bottom	68	52.1 10.4	50.2 8.36	6.61 6.89	35	64.6	0.1	0.3	2326
W1	13	59.8 6.07	58.7 3.88	10.4 5.54	28.1	46.2	22.7	3	572
W2	19	61.0 6.01	58.4 3.69	11.8 5.77	22.8	39.3	26.3	11.7	1001
B1	39	51.5 10.5	50.3 8.57	5.34 6.59	59.9	39.3	0.4	0.4	778
B2	13	53.4 10.1	50.5 7.82	8.97 7.67	29.6	69.5	0	0.9	544
BBL	6	55.02 8.67	52.4 5.79	8.46 6.43	8.8	90.9	0.2	0	803

(c) Diffusive regime (convection)

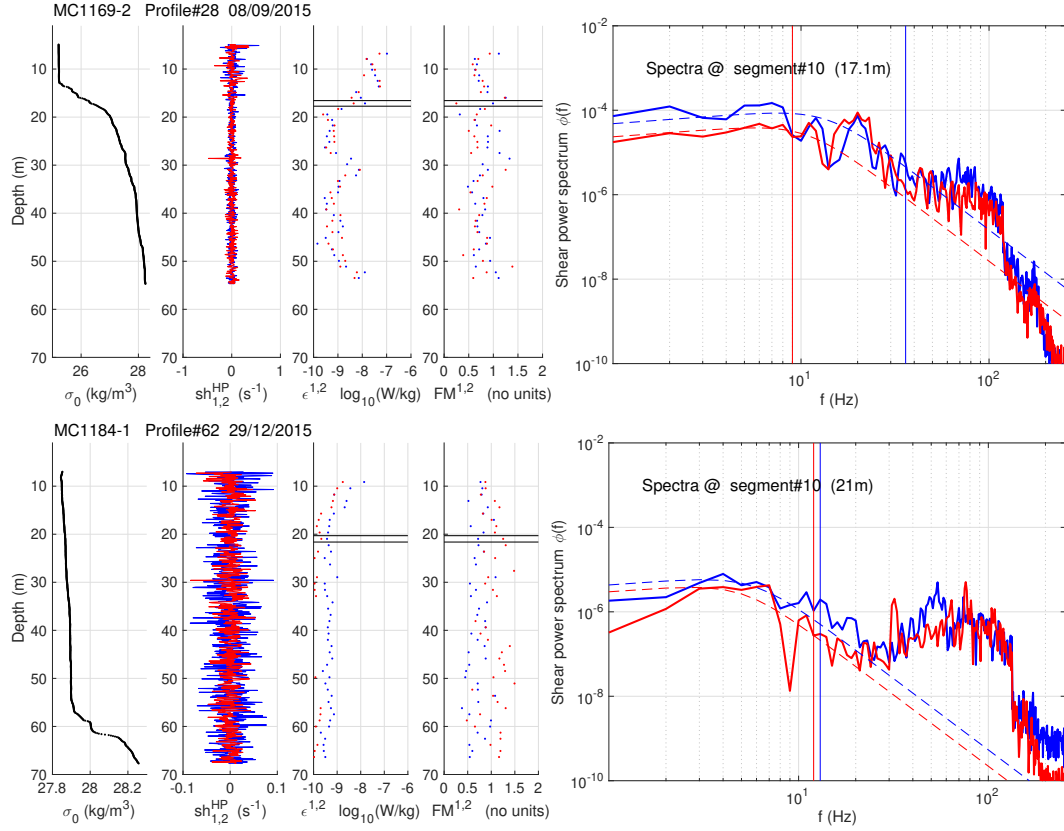| Bin	%	mean Tu mean R_ρ	median	std	SF%	Stable%	Diff.%	Inst.%	Bin count
All	100	-67.4 (Tu) 0.43 (R_ρ)	-67.9 0.42	11.9 0.25	30.8	55.4	10.	3.6	3899
surface-MLD	99	-67.57 0.43	-68.1 0.42	11.8 0.25	24.7	41.8	25	8.5	1573
MLD-bottom	1	-49.3 0.07	-49.1 0.07	3.4 0.06	35	64.6	0.1	0.3	2326
W1	33	-63.6 0.35	-63.0 0.32	10.04 0.20	28.1	46.2	22.7	3	572
W2	66	-69.50 0.48	-71.25 0.49	12.21 0.26	22.80	39.30	26.30	11.70	1001
B1	1	-66.8 0.42	-76.2 0.60	17.6 0.34	59.9	39.3	0.4	0.4	778
B2	0	NaN NaN	NaN NaN	NaN NaN	29.6	69.5	0	0.9	544
BBL	1	-47.6 0.04	-47.6 0.04	2.14 0.03	8.8	90.9	0.2	0	803

Figure S1.   Examples of Nasmyth's spectra fits, for stratified (top) and weakly stratified cases (bottom). The final ϵ is the mean value of the individual estimates ϵ_1 and ϵ_2, excepted for the case where only one value is available (for example after rejection if $FM > 1.5$). Finally, if two estimates differ by one order of magnitude, the lowest is kept.
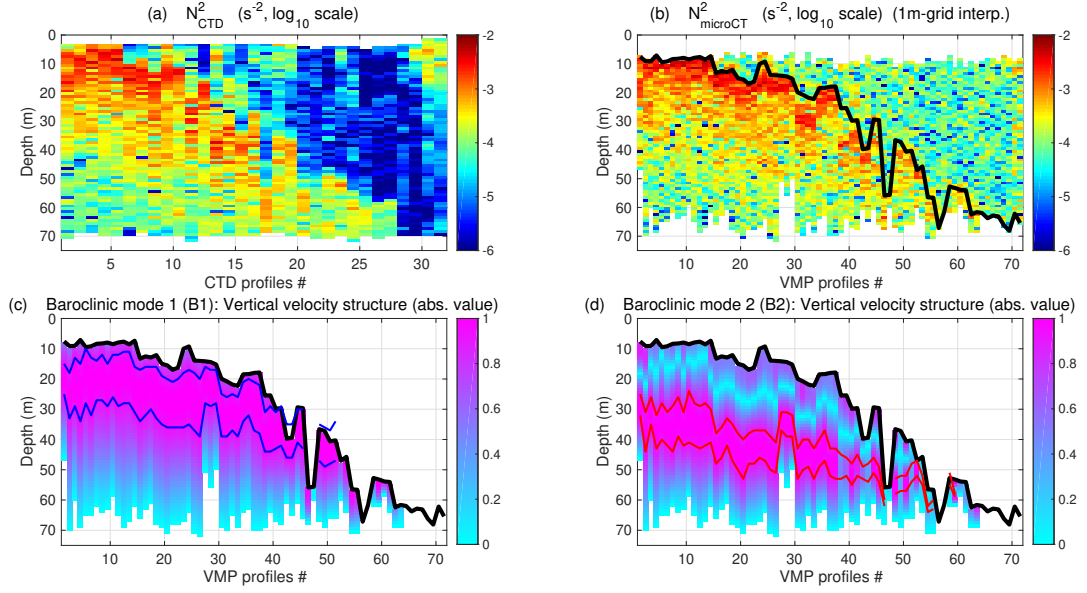
Figure S2. (a) Profiles of the Brunt-Väisälä frequency N^2_{ctd} (s^{-2}) computed from the hydrology obtained with the CTD `Seabird 911+` and (b) N^2_{vmp} (s^{-2}) computed from the hydrology obtained with the micro-CT nose-mounted on the `VMP-250`. Both quantities have been calculated with the dedicated Gibbs Seawater function. $MLD^{\theta}_{0.4°}$ is shown In thick black. (c) Vertical velocity structure (non-dimensional) of the first and (d) second baroclinic modes calculated from N^2_{vmp}. $MLD^{0.4°C}_{\theta_0}$ (thick black line), region of maximum energy of baroclinic mode 1 (between blue lines) and mode 2 (between red lines).

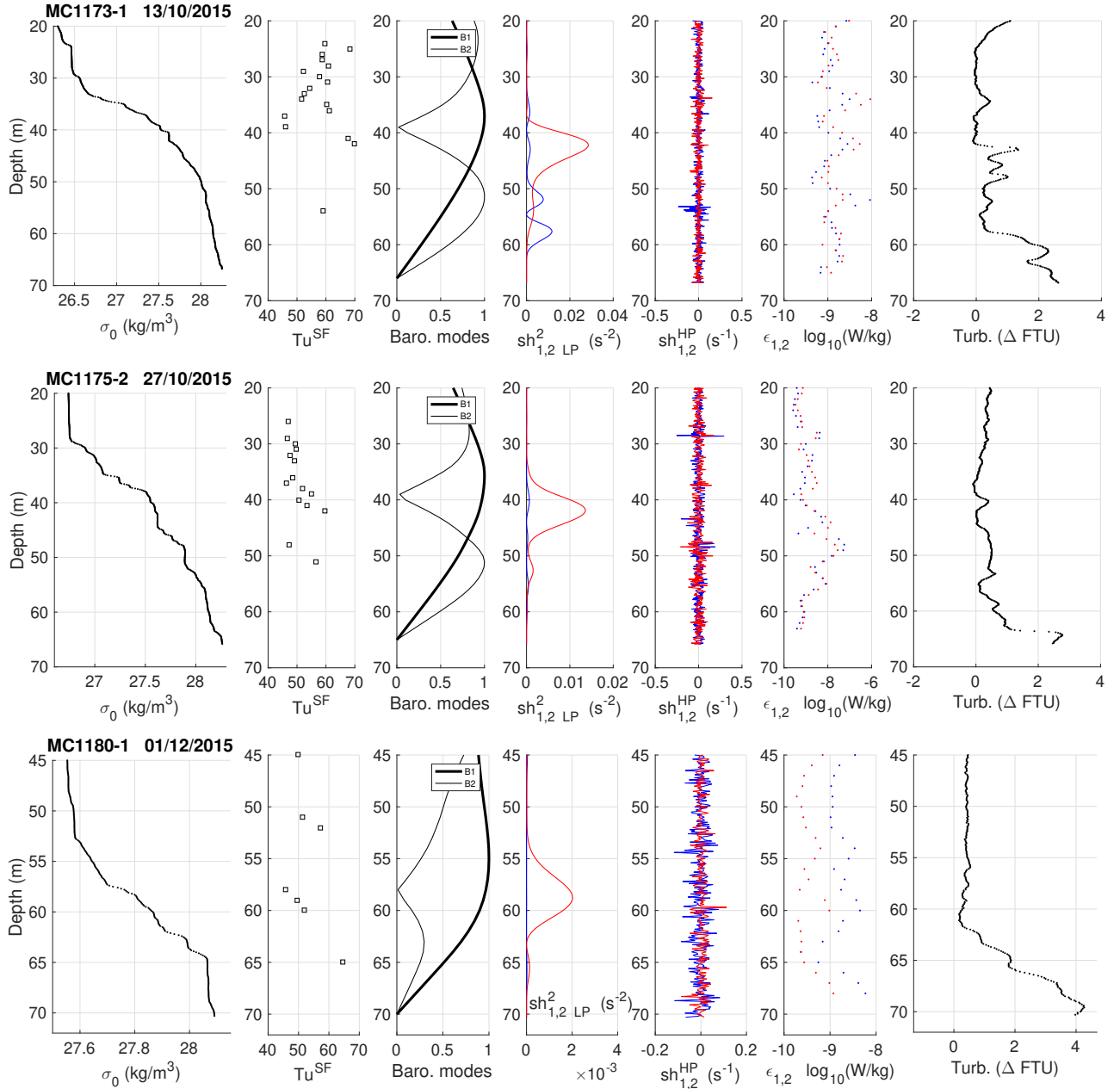**Figure S3.**   Top to bottom : profiles from the VMP casts MC1173, MC1175 and MC1180. From left to right : σ_0 (kg m^{-3}), Turner angles (°) into the salt-fingering regime, first and second vertical baroclinic modes (non-dimensional), low-passed energy shears Sh_{LP} (s^{-2}), hi-passed shears (s^{-1}) used to estimate ϵ (W kg^{-1}), and turbidity (ΔFTU, offset from the reference value -2.5). For shears and ϵ, blue and red refers to the respective shear probes 1 and 2.
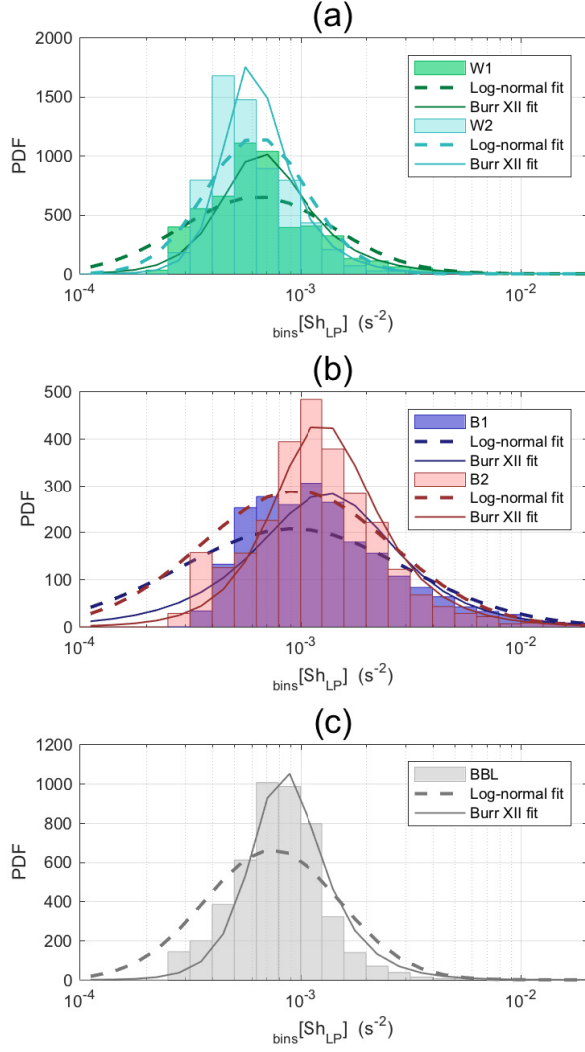
December 1, 2020, 5:45pm

Figure S4. Pdfs of Sh_{LP} i.e. $\langle(\partial_z u)^2\rangle_{LP}^{3m}$ (s^{-2}) through (a) temporal bins W1 and W2, and (b,c) vertical bins B1, B2 and BBL. The fits of the log-normal and Burr type XII distributions are indicated with the dashed and solid lines, respectively.
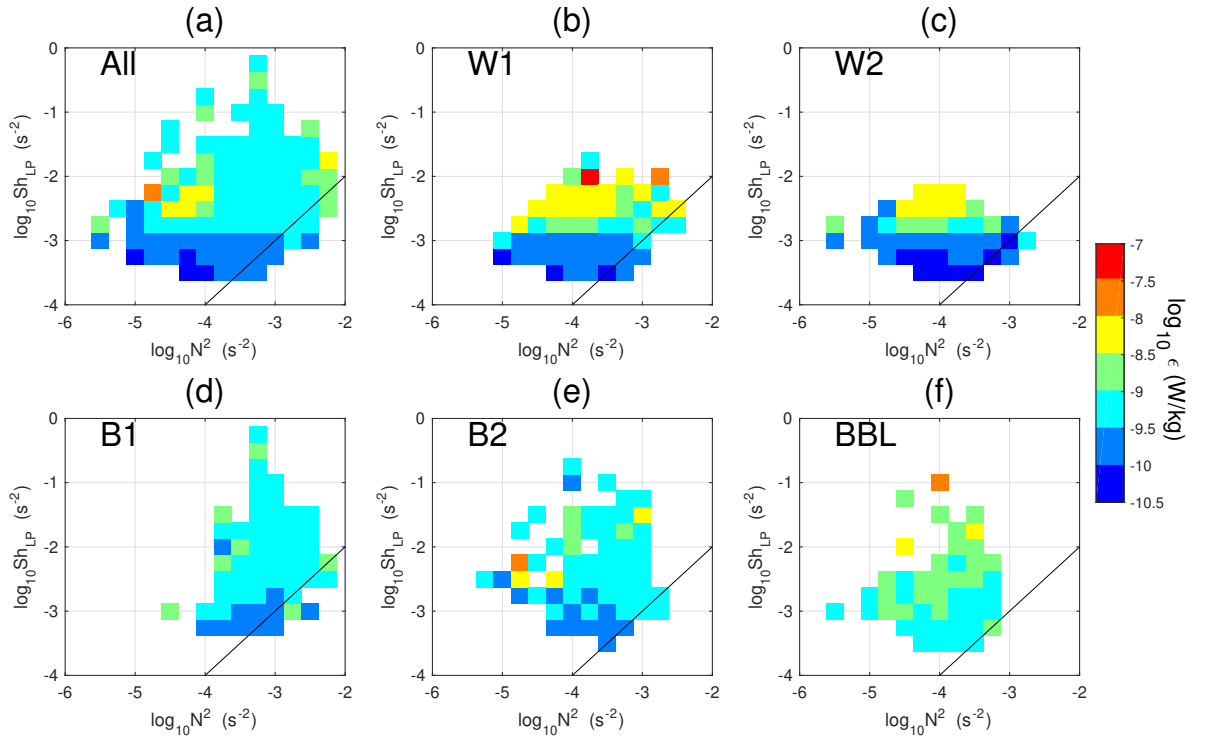
Figure S5. Averaged values of ϵ $(W.kg^{-1})$ by intervals ΔN^2 (s^{-2}) and ΔSh_{LP} (s^{-2}), for the different groups of periods and layers. Intervals ΔN^2 and ΔSh_{LP} have been defined $= 0.25$ in the logarithmic domain (log_{10}). Black line indicates $\frac{N^2}{Sh_{LP}} = 1$.